Received: 18 September 2019 | Revised: 15 January 2020 | Accepted: 16 January 2020
DOI: 10.1002/nbm.4267

WILEY NMR IN BIOMEDICINE

SPECIAL ISSUE RESEARCH ARTICLE

Accuracy and precision of statistical descriptors obtained from multidimensional diffusion signal inversion algorithms

Alexis Reymbaut[1,2] | Paolo Mezzani[1,3] | João P. de Almeida Martins[1,2] | Daniel Topgaard[1,2]

[1]Physical Chemistry Department, Lund University, Lund, Sweden
[2]Random Walk Imaging AB, Lund, Sweden
[3]Physics Department, Università degli Studi di Milano, Milan, Italy

Correspondence
Alexis Reymbaut, PhD, Physical Chemistry Department, Lund University, Naturvetarvägen 14, 22201, Lund, Sweden.
Email: alexis.reymbaut@fkem1.lu.se

Funding information
Stiftelsen för Strategisk Forskning, Grant/Award Number: ITM17-0267; Vetenskapsrådet, Grant/Award Number: 2018-03697

In biological tissues, typical MRI voxels comprise multiple microscopic environments, the local organization of which can be captured by microscopic diffusion tensors. The measured diffusion MRI signal can, therefore, be written as the multidimensional Laplace transform of an intravoxel diffusion tensor distribution (DTD). Tensor-valued diffusion encoding schemes have been designed to probe specific features of the DTD, and several algorithms have been introduced to invert such data and estimate statistical descriptors of the DTD, such as the mean diffusivity, the variance of isotropic diffusivities, and the mean squared diffusion anisotropy. However, the accuracy and precision of these estimations have not been assessed systematically and compared across methods. In this article, we perform and compare such estimations *in silico* for a one-dimensional Gamma fit, a generalized two-term cumulant approach, and two-dimensional and four-dimensional Monte-Carlo-based inversion techniques, using a clinically feasible tensor-valued acquisition scheme. In particular, we compare their performance at different signal-to-noise ratios (SNRs) for voxel contents varying in terms of the aforementioned statistical descriptors, orientational order, and fractions of isotropic and anisotropic components. We find that all inversion techniques share similar precision (except for a lower precision of the two-dimensional Monte Carlo inversion) but differ in terms of accuracy. While the Gamma fit exhibits infinite-SNR biases when the signal deviates strongly from monoexponentiality and is unaffected by orientational order, the generalized cumulant approach shows infinite-SNR biases when this deviation originates from the variance in isotropic diffusivities or from the low orientational order of anisotropic diffusion components. The two-dimensional Monte Carlo inversion shows remarkable accuracy in all systems studied, given that the acquisition scheme possesses enough directions to yield a rotationally invariant powder average. The four-dimensional Monte Carlo inversion presents no infinite-SNR bias, but suffers significantly from noise in the data, while preserving good contrast in most systems investigated.

KEYWORDS
diffusion MRI, *in silico* validation, Laplace inversion, microstructure, tensor-valued diffusion encoding

1 | INTRODUCTION

Diffusion magnetic resonance imaging (dMRI) allows the characterization of living tissues below the millimeter scale set by typical imaging voxel sizes. The basic principle of dMRI techniques is to use magnetic field gradients to encode the acquired signal with information about the

Abbreviations used: 1D, one-dimensional; 2D, two-dimensional; 4D, four-dimensional; Cov, covariance tensor approximation; dMRI, diffusion resonance magnetic resonance imaging; DTD, diffusion tensor distribution; FE, fractional eccentricity; Gamma, Gamma distribution fitting; IQR, interquartile range; MA, microscopic anisotropy index; MC-2D, two-dimensional Monte Carlo inversion; MC-4D, four-dimensional Monte Carlo inversion; MD, mean diffusivity; MK, mean kurtosis; MRI, magnetic resonance imaging; NNLS, nonnegative linear least-squares; SNR, signal-to-noise ratio; μA, microscopic anisotropy; μFA, microscopic fractional anisotropy.

translational motion of water molecules. Restrictions to the measured motion are then used to infer the geometrical configuration of the tissues inside a given voxel. Throughout the signal-encoding process, each water molecule has time to explore a micrometer-scale volume determined by the local diffusivity and the geometry of the cell membranes. The volume explored is only a minor fraction of the available space within the macroscopic imaging voxel, and the dMRI signal is thus a combination of signals arising from multiple microscopic environments with potentially different diffusion properties.[1-4] Classical diffusion observables such as mean diffusivity or fractional anisotropy[5] contain information about the voxel-averaged set of microscopic environments, and can be used to detect changes in the microscopic tissue structure. While voxel-averaged information is readily accessible, resolving the signal contributions from the various microscopic domains is still an open problem that prevents the unambiguous interpretation of in vivo dMRI data in terms of specific tissue properties.[6-9]

In the context of dMRI, the measured signal $\mathcal{S}$ probes diffusion processes over a specific observational time-scale that depends on the choice of experimental time parameters. For a given observational time-scale, a common description of the subvoxel composition of heterogeneous tissues is obtained by considering the combined non-Gaussian diffusion effects of restriction and exchange and approximating the signal decay by a continuous weighted sum of exponential decays,[6,10-29] yielding the following multidimensional Laplace transform:

$$\frac{\mathcal{S}(\mathbf{b})}{\mathcal{S}_0} = \int \mathcal{P}(\mathbf{D}) \exp(-\mathbf{b} : \mathbf{D})\, \mathrm{d}\mathbf{D}\,, \tag{1}$$

where $\mathcal{S}_0$ is the signal acquired when the diffusion encoding gradients have zero amplitude, $\mathcal{P}(\mathbf{D})$ is the distribution of apparent diffusion tensors $\mathbf{D}$ or "diffusion tensor distribution" (DTD) describing an apparent collection of subvoxel diffusion domains,[13] and $\mathbf{b}$ is the diffusion encoding tensor (or b-tensor), an experimental variable that is completely defined by the diffusion-weighting magnetic field gradients.[22,30,31] The b-tensor was introduced in earlier works as a b-matrix accounting for cross terms between diffusion and imaging gradients.[32-34] Here, ":" denotes the Frobenius inner product $\mathbf{b} : \mathbf{D} = \sum_i \sum_j b_{ij} D_{ij}$, and integration spans the space of symmetric positive-semidefinite tensors. Changing the observational time-scale may very well lead to a different set of exponential decays as a result of restricted diffusion[35] and exchange,[36] which implies that the measured DTD may depend on the time-scales or spectral contents of the diffusion-encoding gradients. Even though such time-dependent effects have been measured in human brain white matter,[37-42] spinal cord,[43,44] and prostate,[45,46] using stimulated echo or oscillating gradient sequences specifically designed for varying the observational time-scale over extended ranges, the above DTD description holds for the limited range of time-scales probed by clinical dMRI experiments in the brain.[44,47-54]

While $\mathcal{P}(\mathbf{D})$ provides a simple, and experimentally accessible, description of intravoxel tissue heterogeneity, the inversion of Equation (1) constitutes a challenging ill-posed problem, where clearly distinct distributions may result in signal decays that are indistinguishable within the experimental noise, thus complicating the detailed interpretation of dMRI data. The difficulties posed by the inversion of Equation (1) can be circumvented by fitting the acquired data to intricate signal models, which consider a predefined number of microscopic components and impose *a priori* constraints on the underlying diffusion properties.[19,23-25,28,51,55,56] Alternatively, one can add complexity at the signal acquisition stage in order to encode more information into the diffusion signal and hopefully reduce the number of prior assumptions used to quantify the subvoxel heterogeneity.[31,42,50,57] This idea has motivated the development of tensor-valued diffusion-encoding techniques,[31,58] a number of multidimensional acquisition protocols wherein gradient waveforms are carefully designed to target specific features of $\mathcal{P}(\mathbf{D})$.

The specificity of tensor-valued diffusion encoding is clarified by expanding the Frobenius inner product in Equation (1). To do so, let us assume a distribution of axisymmetric microscopic diffusion tensors $\mathbf{D}$, the axial and radial diffusivities $D_\parallel$ and $D_\perp$ of which, respectively, can be combined to define measures of isotropic diffusivity $D_{\mathrm{iso}} = (D_\parallel + 2D_\perp)/3$ and normalized diffusion anisotropy $D_\Delta = (D_\parallel - D_\perp)/(3D_{\mathrm{iso}}) \in [-0.5, 1]$.[30] The D_{iso} and D_Δ parameters can be interpreted as measures of the "size" and "shape", respectively, of $\mathbf{D}$. Also imposing axisymmetry on the diffusion encoding tensor $\mathbf{b}$ yields[30]

$$\mathbf{b} : \mathbf{D} = bD_{\mathrm{iso}}[1 + 2b_\Delta D_\Delta P_2(\cos\beta)]\,, \tag{2}$$

where $b = \mathrm{Tr}(\mathbf{b})$ is the usual b-value, $b_\Delta \in [-0.5, 1]$ is the normalized anisotropy of $\mathbf{b}$, and $P_2(x) = (3x^2 - 1)/2$ is the second Legendre polynomial. The angle β defines the relative orientation between the diffusion tensor's main axis (θ, ϕ) and the encoding tensor's main axis (Θ, Φ), and is obtained from the spherical law of cosines $\cos\beta = \cos\theta\cos\Theta + \sin\theta\sin\Theta\cos(\phi - \Phi)$. Equation (2) shows clearly that the b_Δ parameter controls the effects of diffusion tensor anisotropy and orientation on the measured signal decay. For instance, setting $b_\Delta = 0$ isolates the effects of D_{iso}, while data acquired at $b_\Delta = 1$ contain the largest possible influence of diffusion anisotropy and orientation. Building upon the specificity of the b_Δ parameter, tensor-valued diffusion encoding techniques compare data acquired at arbitrary $\mathbf{b}$ "shapes" in order to resolve the effects of D_{iso}, D_Δ, and diffusion tensor orientation. By contrast, conventional diffusion encoding schemes are limited to a single $b_\Delta = 1$ value and do not allow control over the influence of diffusion anisotropy on the acquired signal.

Figure 1A presents *in silico* data from two different voxels that are isotropic at the macroscopic scale: one containing a heterogeneous isotropic system (top row), and another one comprising an anisotropic system with low orientational order (bottom row). The displayed data were simulated using a simple protocol comprising multiple b-tensors $\mathbf{b}$ with varying "size" (b), but constant "shape" (b_Δ) and orientation (Θ, Φ). Signals acquired with such protocols are naturally written as the Laplace transform of a 1D distribution of scalar effective diffusivities $\mathcal{P}(D_{\mathrm{eff}})$:[30]

$$\frac{\mathcal{S}(b)}{\mathcal{S}_0} = \int_0^{+\infty} \mathcal{P}(D_{\mathrm{eff}}) \exp\left(-bD_{\mathrm{eff}}\right) \mathrm{d}D_{\mathrm{eff}}\,, \tag{3}$$

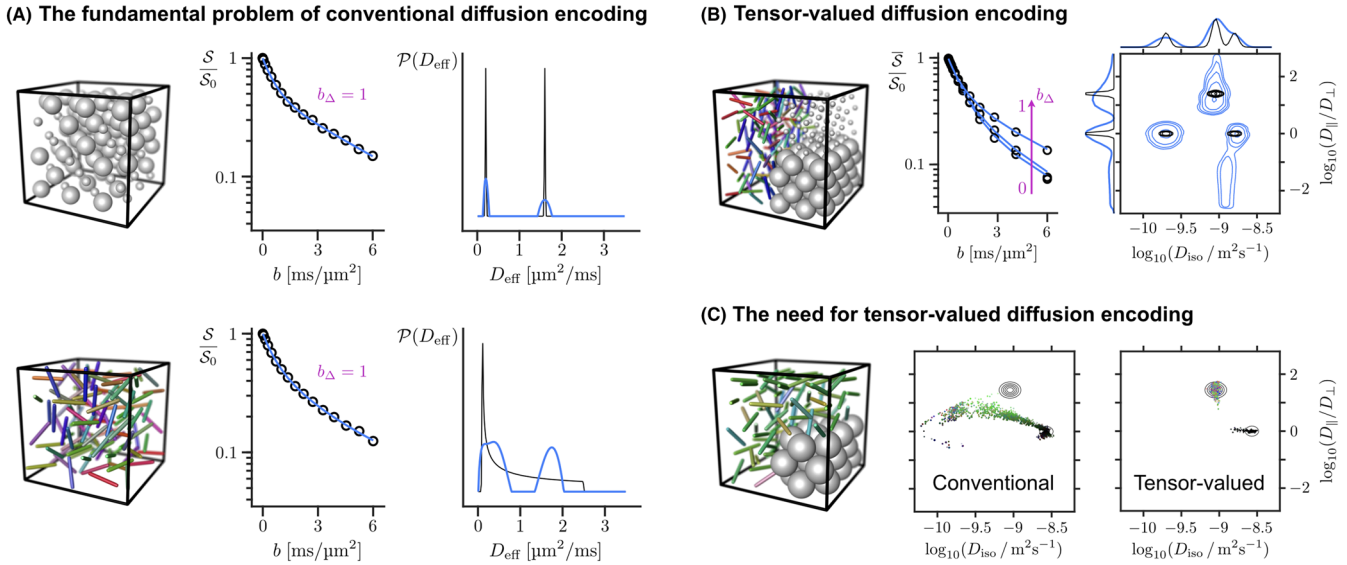

FIGURE 1 Comparison *in silico* between conventional diffusion data and tensor-valued diffusion data in the context of Laplace inversions (SNR = 100). A, From left to right: voxel contents, acquired signal S/S_0 for multiple b-values and constant linear "shape" $b_\Delta = 1$ and orientation (Θ, Φ) (black points), and theoretical distributions of diffusivities $\mathcal{P}(D_{\text{eff}})$ (black lines) associated with different isotropic components (top) and randomly oriented identical anisotropic components (bottom). The isotropic voxel content consists of two equiprobable populations, one with $D_{\text{iso}} = 0.2$ μm^2/ms and the other with $D_{\text{iso}} = 1.6$ μm^2/ms. The anisotropic voxel content is made of components with $D_{\text{iso}} = 0.9$ μm^2/ms and $D_\Delta = 0.89$. The results of a standard Laplace inversion algorithm[59,61] are shown with blue lines. B, Results of the same Laplace inversion algorithm[59,61] on orientationally averaged tensor-valued diffusion-encoded data $\overline{S}(b, b_\Delta)$ Equation (7), inverted via Equation (8) and simulated for a voxel consisting of an equiprobable combination of the two cases in panel A. Such inversion yields a 2D DTD of isotropic diffusivities D_{iso} and anisotropic ratios $D_\parallel/D_\perp = (1 + 2D_\Delta)/(1 - D_\Delta)$.[66] The signals are shown for $b_\Delta = 0$, 0.5, and 1 (from bottom to top, see purple arrow). C, Comparison between the inversions of conventional and tensor-valued diffusion datasets for a voxel containing an isotropic component and an anisotropic component with low orientational order. The isotropic component (25% of the voxel content) has $D_{\text{iso}} = 2.7$ μm^2/ms and the anisotropic component (75% of the voxel content) has $D_{\text{iso}} = 0.9$ μm^2/ms and $D_\Delta = 0.9$. The orientational order of the anisotropic component is set by a Watson distribution of order parameter OP = E$[P_2(\cos\beta)] = 0.2$, where $P_2(x) = (3x^2 - 1)/2$ is the second Legendre polynomial and β is the angle between a component and the main eigenvector of the Saupe order tensor.[69,100] A fair comparison was ensured by considering the same number of input signals and the same SNR for both datasets. Inversions were performed using our 4D Monte Carlo inversion algorithm,[68] yielding a 4D DTD where the unit vectors giving the orientations of the microscopic components are color-coded via the [red, green, blue] $\equiv$ [$|\sin\theta\cos\phi|$, $|\sin\theta\sin\phi|$, $|\cos\theta|$] convention. Ground truth is shown using black contours

where $D_{\text{eff}} \equiv D_{\text{iso}}[1 + 2b_\Delta D_\Delta P_2(\cos\beta)]$. Because the two voxels comprise clearly distinct microscopic structures, their theoretical $\mathcal{P}(D_{\text{eff}})$ distributions have markedly different functional forms. However, in spite of their distinct distributions $\mathcal{P}(D_{\text{eff}})$, the two intravoxel contents yield virtually indistinguishable $b_\Delta = 1$ signals and thus cannot be differentiated with conventional diffusion encoding schemes. Moreover, Laplace inversion algorithms[59-61] cannot reproduce a complex broad distribution $\mathcal{P}(D_{\text{eff}})$ such as the one that characterizes the anisotropic system, and instead yield a solution that bears a higher resemblance to the theoretical distribution of the isotropic system. In the context of dMRI, the different peaks in $\mathcal{P}(D_{\text{eff}})$ may thus be wrongly interpreted as originating from intra- and extracellular water populations. Intuitively, these limitations can be understood via the fact that the one-dimensionality (b) of this simple acquisition protocol does not match the two relevant dimensions $(D_{\text{iso}}, D_\Delta)$ of the physical problem at hand. Figure 1B shows that tensor-valued diffusion encoding circumvents this problem by adding the encoding "shape" b_Δ to the acquisition dimensionality.[62-66] The displayed data were simulated using the orientational average of the diffusion signal (see Equation (7)) and inverted via Equation (8), that is, the orientationally averaged equivalent of Equation (1). Finally, Figure 1C underlines the fact that conventional acquisition schemes sampling multiple directions may not capture the composition of a system that contains isotropic and anisotropic components, even at infinite signal-to-noise ratio (SNR). In other words, this figure demonstrates that the unique information encoded along the b_Δ dimension cannot be replaced by a simple increase in the sampling density of conventional experimental variables. Instead, substituting multiple b_Δ points with more b-values or orientations (Θ, Φ) results in noisy distributions that do not enable a clear separation of the various subvoxel components.

Tensor-valued encoding protocols can be used to encode more information into the acquired signal, but do not correct for the intrinsic ill-posed character of Equation (1). Hence, estimating $\mathcal{P}(\mathbf{D})$ from multidimensional dMRI data acquired at low SNR and comprising a limited number of $(b, b_\Delta, \Theta, \Phi)$ points remains a daunting task in itself. This has led to the development of multiple signal inversion approaches that are mostly distinguished by the amount of information they attempt to extract from $S(\mathbf{b})$.[31] These techniques include nonparametric approaches that attempt to estimate the underlying diffusion tensor distribution,[66-68] and parametric approaches that target statistical descriptors of $\mathcal{P}(\mathbf{D})$ instead of the full distribution.[22,69] Simple and accessible descriptors are the mean isotropic diffusivity

$$\mathrm{E}[D_{\mathrm{iso}}] = \mathrm{MD}\ , \tag{4}$$

the normalized mean squared anisotropy

$$\tilde{\mathrm{E}}[D^2_{\mathrm{aniso}}] = \frac{\mathrm{E}[D^2_{\mathrm{aniso}}]}{\mathrm{E}[D_{\mathrm{iso}}]^2}\ , \tag{5}$$

and the variance of isotropic diffusivities

$$\mathrm{V}[D_{\mathrm{iso}}] = \mathrm{E}[D^2_{\mathrm{iso}}] - \mathrm{E}[D_{\mathrm{iso}}]^2\ , \tag{6}$$

where $D_{\mathrm{aniso}} = D_{\mathrm{iso}} D_\Delta$, and $\mathrm{E}[\,\cdot\,]$ and $\mathrm{V}[\,\cdot\,]$ are the voxel-scale mean and variance, respectively, built from the DTD. These descriptors can be related to quantities derived in previous works: $\mathrm{E}[D_{\mathrm{iso}}]$ is identical to the mean diffusivity (MD); $\tilde{\mathrm{E}}[D^2_{\mathrm{aniso}}]$ carries similar information to the microscopic anisotropy index (MA),[70] the fractional eccentricity (FE),[71] the microscopic anisotropy (μA),[72,73] the normalized difference between second moments $\Delta\tilde{\mu}_2$ and microscopic fractional anisotropy (μFA),[69,72] the anisotropic variance V_{A} and anisotropic mean kurtosis ($\mathrm{MK_A}$),[74,75] and the microscopic anisotropy C_μ;[22] $\mathrm{V}[D_{\mathrm{iso}}]$ yields similar information to the isotropic second moment μ_2^{iso},[69] the isotropic variance V_{I} and isotropic mean kurtosis ($\mathrm{MK_I}$),[74,75] and the normalized isotropic variance C_{MD}.[22] Note that the conventional fractional anisotropy (FA)[5] is a convolution of anisotropy and orientational order, that is, it cannot tease apart the mean squared anisotropic diffusivity $\mathrm{E}[D^2_{\mathrm{aniso}}]$ and the order parameter $\mathrm{OP} = \mathrm{E}[P_2(\cos\beta)]$, as shown in previous work.[69] In fact, tensor-valued diffusion encoding is essential to capture subvoxel anisotropy,[76] reinforcing the conclusions drawn above from Figure 1C. Nevertheless, some caution is required when applying arbitrary gradient waveforms to systems exhibiting restricted diffusion, as directional discrepancies between the frequency contents of these waveforms may cause misestimations of diffusion metrics.[42,77,78] While such misestimations seem challenging to observe on a clinical scanner,[79] they can still be mitigated via "tuning" of the spectral contents.[42,57]

Here, we compare techniques commonly used to invert tensor-valued dMRI data by assessing the accuracy and precision of their estimations of $\mathrm{E}[D_{\mathrm{iso}}]$, $\tilde{\mathrm{E}}[D^2_{\mathrm{aniso}}]$, and $\mathrm{V}[D_{\mathrm{iso}}]$. We focus on four techniques:

- for 2D orientationally averaged signals $\overline{S}(b, b_\Delta)$, the Gamma distribution fitting[69] (Gamma) and the 2D Monte Carlo inversion[66] (MC-2D);
- for 4D signals $S(b, b_\Delta, \Theta, \Phi)$, the covariance tensor approximation[22] (Cov) and the 4D Monte Carlo inversion[67,68] (MC-4D).

The comparison is performed using *in silico* datasets mimicking biologically plausible scenarios, probed with acquisition protocols and SNR levels that are compatible with a clinical setting. Although previous contributions have already reviewed the approaches listed above,[31,58] no rigorous assessment of their performances under clinical experimental conditions has been made so far. In section 2, we lay down the theory of each of the signal inversion techniques investigated. In section 3, we explain how the comparison between these techniques has been carried out. The results are presented and discussed in section 4. Finally, an outlook is given in section 5.

2 | SIGNAL INVERSION APPROACHES

This section offers a pedagogical review of the signal inversion methods investigated in this work, namely the Gamma distribution fitting,[69] the covariance tensor approximation,[22] and the 2D[66] and 4D[67,68] Monte Carlo inversions. Readers with a good understanding of these methods may head directly to section 3.

2.1 | Two-term cumulant expansion of the powder-averaged signal

The dimensionality of the problem stated in Equation (1) can be reduced by averaging data acquired at multiple **b** orientations:[80,81]

$$\overline{S}(b, b_\Delta) = \frac{1}{4\pi}\int_0^{2\pi}\int_0^{\pi} S(b, b_\Delta, \Theta, \Phi)\ \sin\Theta\ \mathrm{d}\Theta\ \mathrm{d}\Phi\ . \tag{7}$$

Known as "powder-averaging",[30,82] this procedure results in a 2D signal that is insensitive to the orientation distribution of the subvoxel environments, and can be written as

$$\overline{S}(b, b_\Delta) = S_0 \int_0^{+\infty} \overline{\mathcal{P}}_{b_\Delta}(D)\ \exp(-bD)\ \mathrm{d}D\ , \tag{8}$$

where our notation of the functional form of the effective distribution $\overline{\mathcal{P}}_{b_\Delta}$ depends explicitly on b_Δ and implicitly on the subvoxel microstructure. General analytical expressions of the powder-averaged signal have been derived recently.[83] This signal corresponds to an integral transform of a joint distribution of isotropic and anisotropic diffusivities, $\mathcal{P}(D_{\mathrm{iso}}, D_\Delta)$, that can be estimated from the data (see Figure 1B).[66] However, much like the original 4D problem, the direct inversion of Equation (8) is a challenging problem that has motivated a number of alternative approaches. For instance, one of the most straightforward ways of extracting information from $\overline{S}(b, b_\Delta)$ consists of approximating Equation (8) with the cumulant expansion of $\overline{\mathcal{P}}_{b_\Delta}$:[30,69,84]

$$\ln\left(\frac{\overline{S}(b, b_\Delta)}{S_0}\right) \underset{b\bar{D}\to 0}{\simeq} -b\bar{D} + b^2\ \frac{\mu_2(b_\Delta)}{2} + \ \dots\ , \tag{9}$$

with the mean $\overline{D} = \int_0^{+\infty} D\, \overline{\mathcal{P}}_{b_\Delta}(D)\, \mathrm{d}D$ and the second cumulant $\mu_2 = \overline{D^2} - \overline{D}^2$. This expansion is only valid for $b\overline{D} \to 0$, which explains why it is commonly cut at the second order, as higher-order terms are negligible in that limit, yielding the two-term cumulant expansion

$$\ln\left(\frac{\overline{S}(b, b_\Delta)}{S_0}\right) \underset{b\bar{D}\to 0}{\simeq} -b\bar{D} + b^2\, \frac{\mu_2(b_\Delta)}{2}\,. \tag{10}$$

By fitting the measured signal to Equation (10), using S_0, $\overline{D}$, and μ_2 as fitting variables, one can target statistical measures of $\overline{\mathcal{P}}_{b_\Delta}(D)$ directly without having to either retrieve the full distribution or define its explicit functional form. From the cumulant expansion, it is clear that signal deviations from monoexponentiality are described at low b-values by the second central moment μ_2. These deviations may come from intravoxel variance in isotropic diffusivities or from anisotropy, and their effects on the powder-averaged signal can be teased apart by the encoding anisotropy b_Δ, as μ_2 can be written as[30]

$$\mu_2(b_\Delta) = \mathrm{V}[D_{\mathrm{iso}}] + \frac{4b_\Delta^2}{5}\, \mathrm{E}[D_{\mathrm{aniso}}^2]\,. \tag{11}$$

Within this formalism, one has

$$\mathrm{E}[D_{\mathrm{iso}}] = \overline{D}\,, \tag{12}$$

$$\mathrm{V}[D_{\mathrm{iso}}] = \mu_2(b_\Delta = 0)\,, \tag{13}$$

$$\mathrm{E}[D_{\mathrm{aniso}}^2] = \frac{5}{4}\,[\mu_2(b_\Delta = 1) - \mu_2(b_\Delta = 0)]\,. \tag{14}$$

Even though the cumulant approach seems very direct for microstructural studies, it is inherently limited to small values of $b\overline{D}$. Importantly, this means that adding more terms to Equation (10) (in the spirit of Equation (9)) will not significantly improve the adequacy of the cumulant expansion to describe systems where higher-order moments of $\overline{\mathcal{P}}_{b_\Delta}(D)$ are significant, such as ensembles of orientationally dispersed anisotropic components (see the bottom panel of Figure 1A).

2.2 | Gamma distribution fitting (Gamma)

The problem of inverting $\overline{S}(b, b_\Delta)$ (see Equation (7)) can instead be formulated as finding a physically plausible approximation of $\overline{\mathcal{P}}_{b_\Delta}$. The Gamma distribution function has been shown to provide a good approximation:[85]

$$\mathcal{P}_\Gamma(D, \kappa, \psi) = \frac{D^{\kappa-1}}{\psi^\kappa\, \Gamma(\kappa)}\, \exp(-D/\psi)\,, \tag{15}$$

where κ is the unitless shape parameter, ψ is a scale parameter with diffusivity units, and Γ denotes the Gamma function. This analytical form of $\overline{\mathcal{P}}_{b_\Delta}$ is practical, because it is described by a minimal number of parameters and possesses a simple analytical Laplace transform: $\overline{S}(b, \kappa, \psi)/S_0 = (1 + b\psi)^{-\kappa}$. Using the fact that the Gamma distribution gives $\overline{D} = \kappa\psi$ and $\mu_2 = \kappa\psi^2$, one obtains the analytical expression[69]

$$\frac{\overline{S}(b, b_\Delta)}{S_0} = \left(1 + b\, \frac{\mu_2(b_\Delta)}{\overline{D}}\right)^{-\overline{D}^2/\mu_2(b_\Delta)}\,, \tag{16}$$

the fit of which provides $\overline{D}$ and $\mu_2(b_\Delta)$ for microstructural estimation of the metrics Equations (12), (13), and (14). It is important to mention that the Gamma distribution fitting implemented in this work is performed on the entire dataset and features a soft Heaviside signal-weighting function that limits the fit to the range where the signal attenuation does not reach a reasonable noise floor, as used in previous works.[74,86]

2.3 | Covariance tensor approximation (Cov)

The two-term cumulant expansion Equation (10) can be generalized to non powder-averaged signals as the covariance tensor approximation:[22]

$$\ln\left(\frac{S}{S_0}\right) \underset{\mathbf{b}:\langle\mathbf{D}\rangle\to 0}{\simeq} -\mathbf{b} : \langle\mathbf{D}\rangle + \frac{1}{2}\, \mathbf{b}^{\otimes 2} : \mathbb{C}\,, \tag{17}$$

with the voxel-scale averaged diffusion tensor $\langle\mathbf{D}\rangle$, the outer tensor product $\otimes$ such that $\mathbf{b}^{\otimes 2} = \mathbf{b} \otimes \mathbf{b}$, and the 6×6 covariance tensor $\mathbb{C} = \langle\mathbf{D}^{\otimes 2}\rangle - \langle\mathbf{D}\rangle^{\otimes 2}$ in Mandel notation. This approximation is equivalent to considering a normal distribution of diffusion tensors. However, the fact that this distribution allows for negative-definite tensors implies that negative values can be found for the positive quantities described in section 3.2. The aforementioned metrics Equations (12), (13), and (14) can then be expressed in terms of tensor inner and outer products involving the voxel-scale averaged diffusion tensor and the covariance tensor. Indeed, let us introduce the isotropic tensors $\mathbf{E}_{\mathrm{iso}} = \mathbf{I}_3/3$ and

$\mathbb{E}_{\text{iso}} = \mathbf{I}_6/3$, where $\mathbf{I}_n$ is the $n \times n$ identity matrix. Using the Mandel notation, in which a 3×3 symmetric tensor Λ can be written as the column vector $(\lambda_{xx} \;\; \lambda_{yy} \;\; \lambda_{zz} \;\; \sqrt{2}\lambda_{yz} \;\; \sqrt{2}\lambda_{xz} \;\; \sqrt{2}\lambda_{xy})^{\mathsf{T}}$, one builds the bulk and shear modulus tensors,

$$\mathbb{E}_{\text{bulk}} = \mathbf{E}_{\text{iso}}^{\otimes 2} = \frac{1}{9}\begin{pmatrix} 1 & 1 & 1 & 0 & 0 & 0 \\ 1 & 1 & 1 & 0 & 0 & 0 \\ 1 & 1 & 1 & 0 & 0 & 0 \\ 0 & 0 & 0 & 0 & 0 & 0 \\ 0 & 0 & 0 & 0 & 0 & 0 \\ 0 & 0 & 0 & 0 & 0 & 0 \end{pmatrix} \quad , \quad \mathbb{E}_{\text{shear}} = \mathbb{E}_{\text{iso}} - \mathbb{E}_{\text{bulk}} = \frac{1}{9}\begin{pmatrix} 2 & -1 & -1 & 0 & 0 & 0 \\ -1 & 2 & -1 & 0 & 0 & 0 \\ -1 & -1 & 2 & 0 & 0 & 0 \\ 0 & 0 & 0 & 3 & 0 & 0 \\ 0 & 0 & 0 & 0 & 3 & 0 \\ 0 & 0 & 0 & 0 & 0 & 3 \end{pmatrix} , \tag{18}$$

by analogy with the stress tensor in mechanics, and obtains

$$\mathrm{E}[D_{\text{iso}}] = \langle \mathbf{D} \rangle : \mathbf{E}_{\text{iso}} \; , \tag{19}$$

$$\mathrm{V}[D_{\text{iso}}] = \mathbb{C} : \mathbb{E}_{\text{bulk}} \; , \tag{20}$$

$$\mathrm{E}[D_{\text{aniso}}^2] = \frac{(\mathbb{C} + \langle \mathbf{D} \rangle^{\otimes 2}) : \mathbb{E}_{\text{shear}}}{2} = \frac{\langle \mathbf{D}^{\otimes 2} \rangle : \mathbb{E}_{\text{shear}}}{2} \; . \tag{21}$$

The list of fitting parameters includes $\mathcal{S}_0$, the six independent elements of $\langle \mathbf{D} \rangle$, and the 21 independent elements of $\mathbb{C}$, which makes a total of 28 parameters to estimate within this approximation. Consequently, the covariance tensor approximation requires the acquisition of multiple signals over a wide range of b-tensor sizes, shapes, and orientations in order to be reliable. The main advantage of the covariance tensor approximation is that it yields very fast inversions, as Equation (17) can be recast into a linear problem tractable via mere matrix pseudoinversion. However, this approach's limitation to small values of $\mathbf{b} : \langle \mathbf{D} \rangle$ prevents it from accurately capturing the microstructural features of systems where higher-order moments of the underlying DTD are significant, such as ensembles of orientationally dispersed anisotropic components (see the bottom panel of Figure 1A).

Figure 2 shows that the Gamma (Equation (16)) and covariance (Equation (17)) approaches may not be able to capture the features of the DTD $\mathcal{P}(\mathbf{D})$ accurately, even at infinite SNR. Used as forward models, they can yield biased signals; used to solve an inverse problem, they can yield biased statistical descriptors.

2.4 | Monte Carlo inversion (MC-2D and MC-4D)

To facilitate its numerical inversion, the continuous distribution $\mathcal{P}(\mathbf{D})$ can be approximated by a discrete vector $\mathbf{w}$ containing the weights of N distinct diffusion tensors. This allows us to rewrite Equation (1) as

$$\mathcal{S}_m = \sum_{n=1}^{N} w_n \; K(\mathbf{b}_m, \mathbf{D}_n) \; , \tag{22}$$

where $\mathcal{S}_m$ is the mth signal amplitude measured with the encoding tensor $\mathbf{b}_m$, and w_n is the weight of the nth point from the discretized DTD space. The analysis $\mathbf{D}_n$ and acquisition $\mathbf{b}_m$ spaces are linked by the generalized inversion kernel K, the analytical form of which is determined by the experimental design. For 4D signals $\mathcal{S}(\mathbf{b})$, the inversion kernel is determined by Equation (2),

$$K_{mn}^{(4\text{D})} = \exp(-b_m D_{\text{iso},n}[1 + 2b_{\Delta,m} D_{\Delta,n} P_2(\cos \beta_{mn})]) \; , \tag{23}$$

whereas for 2D powder-averaged signals $\overline{\mathcal{S}}(b, b_\Delta)$ the kernel can be shown to be equal to[30]

$$K_{mn}^{(2\text{D})} = \sqrt{\frac{\pi}{2}} \, \frac{\operatorname{erf}(\sqrt{3 b_m b_{\Delta,m} D_{\text{iso},n} D_{\Delta,n}})}{\sqrt{3 b_m b_{\Delta,m} D_{\text{iso},n} D_{\Delta,n}}} \, \exp(-b_m D_{\text{iso},n}[1 - b_{\Delta,m} D_{\Delta,n}]) \; , \tag{24}$$

with $\operatorname{erf}(\cdot)$ denoting the error function. Since the number of experimental points, M, is typically higher than the number of unknowns, N, Equation (**?**) represents an overdetermined system. The estimation of $\mathbf{w}$ is thus formulated as a nonnegative linear least-squares (NNLS) problem:

$$\mathbf{w} = \underset{\mathbf{w} \geq 0}{\operatorname{argmin}} \; \|\mathbf{s} - \mathbf{K} \cdot \mathbf{w}\|_2 \; , \tag{25}$$

where $\|\cdot\|_2$ denotes the Euclidian norm, $\mathbf{w}$ is the $N \times 1$ sought-for probability vector, $\mathbf{s}$ is the $M \times 1$ vector containing the signal amplitude measurements, and $\mathbf{K}$ is the $M \times N$ matrix approximation of the appropriate inversion kernel.

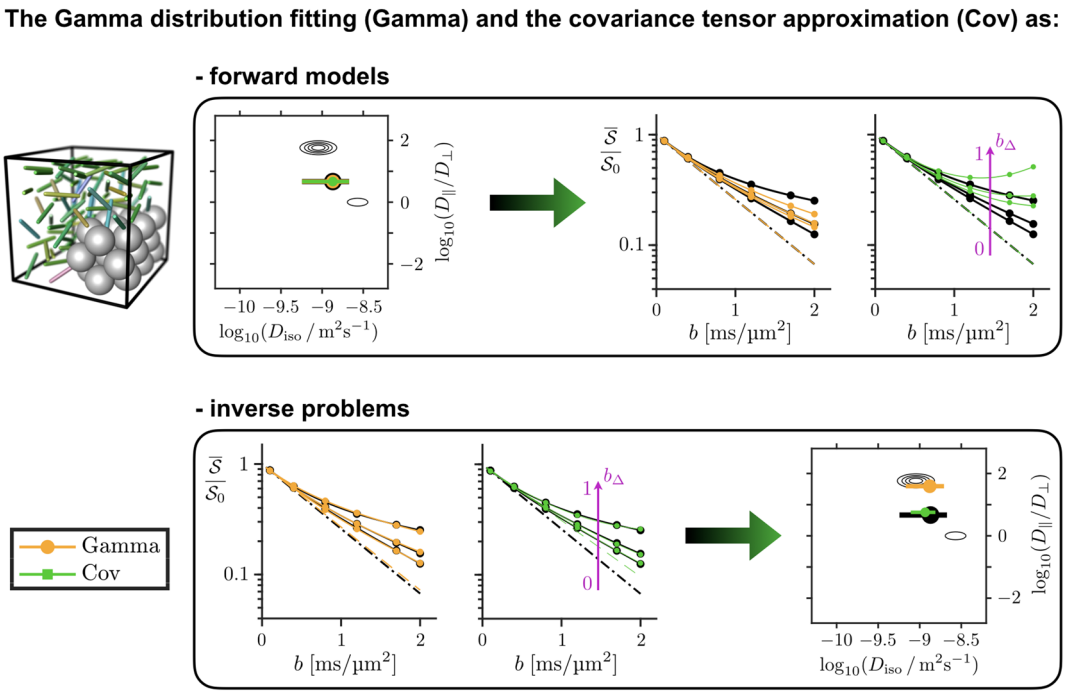

FIGURE 2 Comparison at infinite SNR between typical results yielded by the Gamma distribution fitting (orange), the covariance tensor approximation (green), and the ground-truth signals/statistical descriptors (black) obtained for the same voxel content as in Figure 1C. In the signal panels, the colored solid lines denote the signal decays estimated from the various methods and the colored dashed lines correspond to their initial slopes, which are regulated by the estimated mean diffusivities. In the square DTD panels, colored points represent the logarithms of $\mathrm{E}[D_{iso}]$ and $\mathrm{E}[D_\parallel/D_\perp]$, and the horizontal line reflects the standard deviation of isotropic diffusivities. Since D_Δ is not directly accessible for Gamma and Cov, we defined $\mathrm{E}[D_\parallel/D_\perp] = (1 + 2\tilde{\mathrm{E}}[D_\Delta])/(1 - \tilde{\mathrm{E}}[D_\Delta])$, where $\tilde{\mathrm{E}}[D_\Delta] = \sqrt{\mathrm{E}[D^2_{aniso}]/\mathrm{E}[D_{iso}]^2} = \sqrt{\mathrm{E}[D^2_{iso}D^2_\Delta]/\mathrm{E}[D_{iso}]^2}$. The performances of Gamma and Cov are illustrated here for both the forward problem (top), where the ground-truth statistical descriptors are used to compute the signals predicted by the inversion methods, and the inverse problem (bottom), where the ground-truth signals are inverted to estimate the statistical descriptors. The signals are shown for $b_\Delta = 0$, 0.5, and 1 (from bottom to top, see purple arrows), as in Figure 1B

Inverting an ill-posed system of linear equations such as the one described by Equation (25) is a rather common task for a wide array of scientific disciplines.[87] Within the field of magnetic resonance, this class of problems is particularly relevant, as the analysis of relaxation or diffusion data can generally be formulated as an inversion of a discrete vector describing the amplitudes of multiple exponential decays. The ubiquity of the problem explains the abundance of methods that can be used to invert Equation (25), in both general[59,87] and magnetic resonance[61,88-91] literature. In this work, we opted for iterative Monte Carlo algorithms that were specially designed to handle high-dimensional datasets:[66-68] MC-2D and MC-4D. While MC-2D is used to estimate $\mathcal{P}(D_{iso}, D_\Delta)$ from powder-averaged signals, MC-4D is used to estimate $\mathcal{P}(D_{iso}, D_\Delta, \theta, \phi)$ from non-powder-averaged signals.

The Monte Carlo inversion process was described in detail in previous works,[67,68] and is schematized in Figure 3. As a first step, the algorithm selects a random set $\{\mathbf{D}_n\}_{1\leq n\leq N_{in}}$ of N_{in} diffusional configurations and subsequently estimates the corresponding set of weights $\{w_n\}_{1\leq n\leq N_{in}}$ via a NNLS minimization routine, storing the configurations with $w_n > 0$. This process, called "proliferation", is repeated for N_p distinct rounds, after which the final set $\{\mathbf{D}_n\}$ of $w_n > 0$ configurations is stored and subjected to a small random perturbation, called "mutation". This marks the beginning of the "extinction" step, wherein diffusion configurations compete with their respective mutations on the basis of the lowest residual sums of squares. The mutation and extinction steps are repeated N_m times. Finally, the N_{out} configurations with highest weights are taken as a solution of Equation (22). In this work we used $N_{in} = 100$, $N_p = 20$ (MC-2D) and 10 (MC-4D), $N_m = 20$ (MC-2D) and 10 (MC-4D), and $N_{out} = 50$. The initial configurations of MC-2D were randomly generated within the bounds $-11 \leq \log_{10}(D_\parallel/m^2s^{-1}) \leq -8.3$ and $-11 \leq \log_{10}(D_\perp/m^2s^{-1}) \leq -8.3$. As for MC-4D's initial configurations, they were sampled within the bounds $-11 \leq \log_{10}(D_\parallel/m^2s^{-1}) \leq -8.3$, $-11 \leq \log_{10}(D_\perp/m^2s^{-1}) \leq -8.3$, $0 \leq \cos(\theta) \leq 1$, and $0 \leq \phi \leq 2\pi$. By construction, this approach is not limited in terms of the cumulants that it can estimate, since any cumulant can be computed from means, variances, covariances, or higher-order statistics of the diffusional properties of the configurations. Besides, since the Monte Carlo inversions build up the DTD as a sum of components, they enable a natural separation of subvoxel tissues.[92] It should be mentioned that the additional information provided by these algorithms comes at a cost in computational time: as implemented in Matlab,[93,94] the iterative Monte Carlo approaches are twice as slow as the Gamma distribution fitting and 60–80 times slower than the covariance tensor approximation.

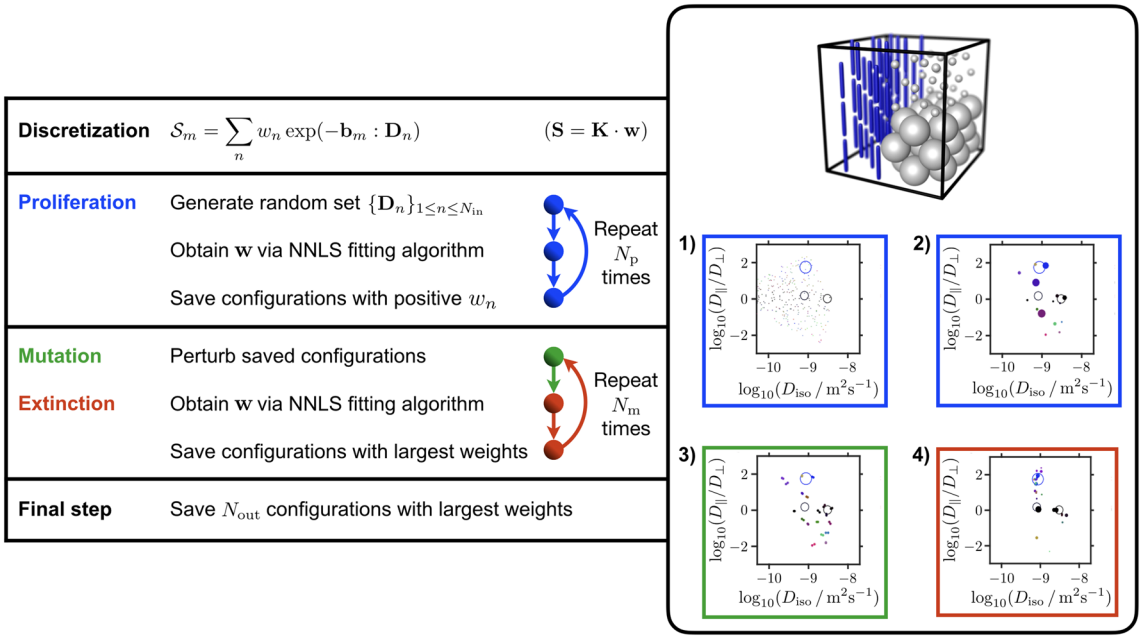

FIGURE 3 Illustration of the 4D Monte Carlo algorithm for Laplace inversion. *Left*, Main steps of the inversion algorithm. *Right*, Practical example of the the inversion algorithm for a voxel containing one anisotropic component and two distinct isotropic components. The diffusion tensor distribution (DTD) is represented at various steps of the inversion algorithm as 2D bubble charts of $\log_{10}(D_{iso})$ and $\log_{10}(D_\parallel/D_\perp)$, where diffusion orientation is color-coded via the [red, green, blue] $\equiv$ [$|\sin\theta\cos\phi|$, $|\sin\theta\sin\phi|$, $|\cos\theta|$] convention. While empty circles show the ground-truth solutions, filled circles show the investigated configurations (circle radii encoded for the associated probability weights). First, the set of acquired signals (index m) is discretized following Equation (22). The index n denotes the different random configurations generated at the beginning of the proliferation step (box 1). Each of these N_{in} configurations is given a probability weight w_n through the NNLS minimization Equation (25) and survives the proliferation step if $w_n > 0$. After N_p repetitions of this step (box 2), the stability of the saved solutions is tested by randomly perturbing (mutating) them and estimating the probability weights of the new perturbed solutions (box 3). The extinction step saves the configurations of highest probability (box 4). After N_m repetitions of the mutation and extinction steps, the N_{out} configurations with the largest weights are taken as a solution of Equation (22)

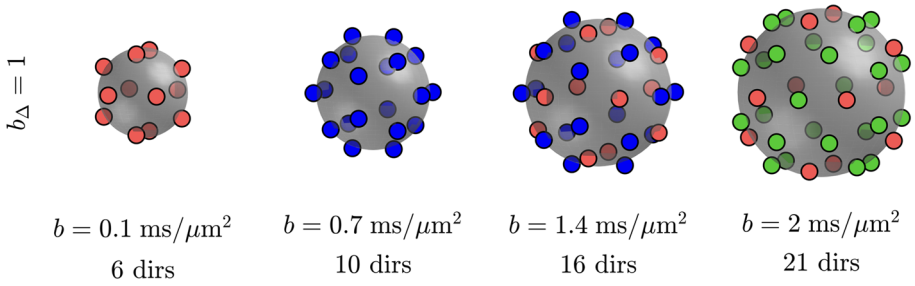

FIGURE 4 Direction sets used for the $b_\Delta = 1$ dataset. Different colors represent directions derived from different platonic solids[22]

3 | METHODS

3.1 | Simulated acquisition schemes

We considered an abbreviated **b** acquisition scheme that can be readily implemented in a standard clinical MRI scanner as a 6–7 minute protocol comprising 30 axial slices. Similar protocols have already been used for in vivo studies of brain tissue microstructure.[95] The acquisition scheme consists of 53 linearly encoded signals ($b_\Delta = 1$) distributed over four b-values (6, 10, 16, and 21 points at b = 100, 700, 1400, and 2000 s/mm^2, respectively), 32 spherically encoded signals ($b_\Delta = 0$) sampled over four b-values (6, 6, 10, and 10 points at b = 100, 700, 1400, and 2000 s/mm^2, respectively), plus one $b = 0$ signal. The various points of the $b_\Delta = 1$ dataset were measured at different **b** orientations. For each b shell, we used direction sets derived from platonic solids,[22] as shown in Figure 4. The number of directions per shell was chosen in order to yield a rotationally invariant powder-averaged signal.[95]

3.2 | Statistical descriptors

According to Equations (10) and (11), the powder-averaged signal deviations from monoexponentiality have a first-order dependence on the voxel-scale variance of isotropic diffusivities V[D_{iso}] and the voxel-scale mean of squared anisotropic diffusivities E[D^2_{aniso}]. Therefore, we focus on the estimation of the mean diffusivity E[D_{iso}] (Equation (4)), the normalized mean squared anisotropy $\tilde{\mathrm{E}}[D^2_{aniso}]$ (Equation (5)), and the isotropic

variance V[D_{iso}] (Equation (6)). While these statistical descriptors are all lower-bounded by 0, the mean diffusivity is reasonably upper-bounded by the free-water diffusivity, that is, 3 μm^2/ms at body temperature, the normalized mean anisotropy is upper-bounded by 1 by construction, and the isotropic variance is reasonably upper-bounded around 1.21 μm^4/ms^2 for a voxel containing equal proportions of free water ($D_{iso} \simeq 3$ μm^2/ms) and white matter ($D_{iso} \simeq 0.8$ μm^2/ms).

3.3 | Comparison steps

To ensure a fair comparison of the different inversion techniques, all readily available as Matlab code on GitHub,[93,94] we follow the steps below.

1. A system of interest is simulated by generating a set of ground-truth features $\{D_{\parallel}, D_{\perp}, \theta, \phi, w\}$, from which the ground-truth descriptors of interest and the ground-truth set of signals $\{S_{gt,i}\}$ are computed using the general signal decay Equation (1). This computation is in agreement with the conventional procedure for testing 1D or 2D Laplace inversion algorithms, where the ground-truth signal is calculated with the same kernel as the inversion and it is well known that infinite SNR is not by itself sufficient for recovering the input distribution.[59,61,89,91]
2. Each signal inversion technique is run on an identical set of signals with added Rician noise:

$$\{S_i\} = \left\{ \sqrt{\left(S_{gt,i} + \frac{\nu_i}{SNR}\right)^2 + \left(\frac{\nu_i'}{SNR}\right)^2} \right\}, \tag{26}$$

   where ν_i and ν_i' denote random numbers drawn from a normal distribution with zero mean.
3. Step 2 is repeated 100 times to build up statistics on parameter estimation of E[D_{iso}], $\tilde{E}[D_{aniso}^2]$, and V[D_{iso}].

In this work, we investigated a clinically relevant SNR of 30 and the ideal infinite SNR. Since the Rician bias has been shown to be relevant only when the SNR approaches unity,[96] affecting the estimation of diffusion metrics,[97-99] the results presented in section 4 are identical to those obtained from signals with added Gaussian noise. While accuracy is quantified by the difference between the median and the ground-truth (bias), precision is quantified by the interquartile range (IQR). A "good" estimation is defined as one that presents both high accuracy and high precision.

4 | RESULTS AND DISCUSSION

4.1 | Varying mean diffusivity

Figure 5 shows the accuracy and precision of the investigated signal inversion algorithms for isotropic unimodal systems with various mean diffusivities E[D_{iso}], probed with the acquisition scheme described in section 3.1. Gamma and Cov, two methods that consider a fixed functional form for the DTD, behave differently when E[D_{iso}] varies. Indeed, while Gamma shows excellent accuracy and precision for all values of E[D_{iso}], Cov estimates a negative normalized anisotropy and presents finite-SNR biases in E[D_{iso}] and V[D_{iso}] at high E[D_{iso}] values. Such biases come from the fact that higher mean diffusivities at constant maximal b-value push the covariance tensor approximation further beyond its range of validity in terms of the value of $\mathbf{b} : \langle \mathbf{D} \rangle$ (see Equation (17)), making it more sensitive to noise in the data without necessarily making it inadequate at higher SNRs (absence of infinite-SNR bias). As for MC-2D, which does not consider a fixed functional form for the powder-averaged DTD, it correctly quantifies changes caused by E[D_{iso}], albeit with a low precision in V[D_{iso}]. Finally, MC-4D, which does not consider a fixed functional form for the general DTD, overestimates $\tilde{E}[D_{aniso}^2]$ significantly at finite SNR, but preserves contrast for E[D_{iso}] and V[D_{iso}] nonetheless. This overestimation, along with the absence of infinite-SNR bias in $\tilde{E}[D_{aniso}^2]$, indicates a high sensitivity of MC-4D to noise in the acquired signals. In Figure 5 and all remaining figures of this work, a general trend is that any bias in estimating the mean diffusivity E[D_{iso}] is reflected directly as a bias in estimating the other isotropic descriptor, that is, the isotropic variance V[D_{iso}]. In contrast, the estimation of the mean normalized anisotropy $\tilde{E}[D_{aniso}^2]$ is quite independent of the other descriptor estimations.

4.2 | Varying variance of isotropic diffusivities

Figure 6 shows the accuracy and precision of the signal inversion algorithms investigated for isotropic bimodal systems that change in terms of isotropic variance V[D_{iso}], while keeping a constant low E[D_{iso}] of 0.8 μm^2/ms (panel A) or a constant high E[D_{iso}] of 2 μm^2/ms (panel B). Both cases are relevant in vivo: while the former could arise in diseased white matter, the latter represents voxels containing both low E[D_{iso}] tissues, such as white or grey matter, and high E[D_{iso}] environments, such as cerebrospinal fluid or edema. It is worth noting that using unimodal distributions to generate isotropic variance in the ground-truth DTD yields the same results as those obtained from bimodal distributions. However, unimodal distributions implemented within physical bounds are limited to a narrower range of isotropic variances.

At infinite SNR, both Gamma and Cov present biases in estimating E[D_{iso}] and V[D_{iso}] at low E[D_{iso}] and high V[D_{iso}]. Although the Cov approach possesses a higher precision in that regime, it also displays much larger infinite-SNR biases than Gamma at high E[D_{iso}] and high V[D_{iso}]. The infinite-SNR biases observed at low E[D_{iso}] and high V[D_{iso}] persist at finite SNR. The infinite-SNR biases of Cov at high E[D_{iso}] are

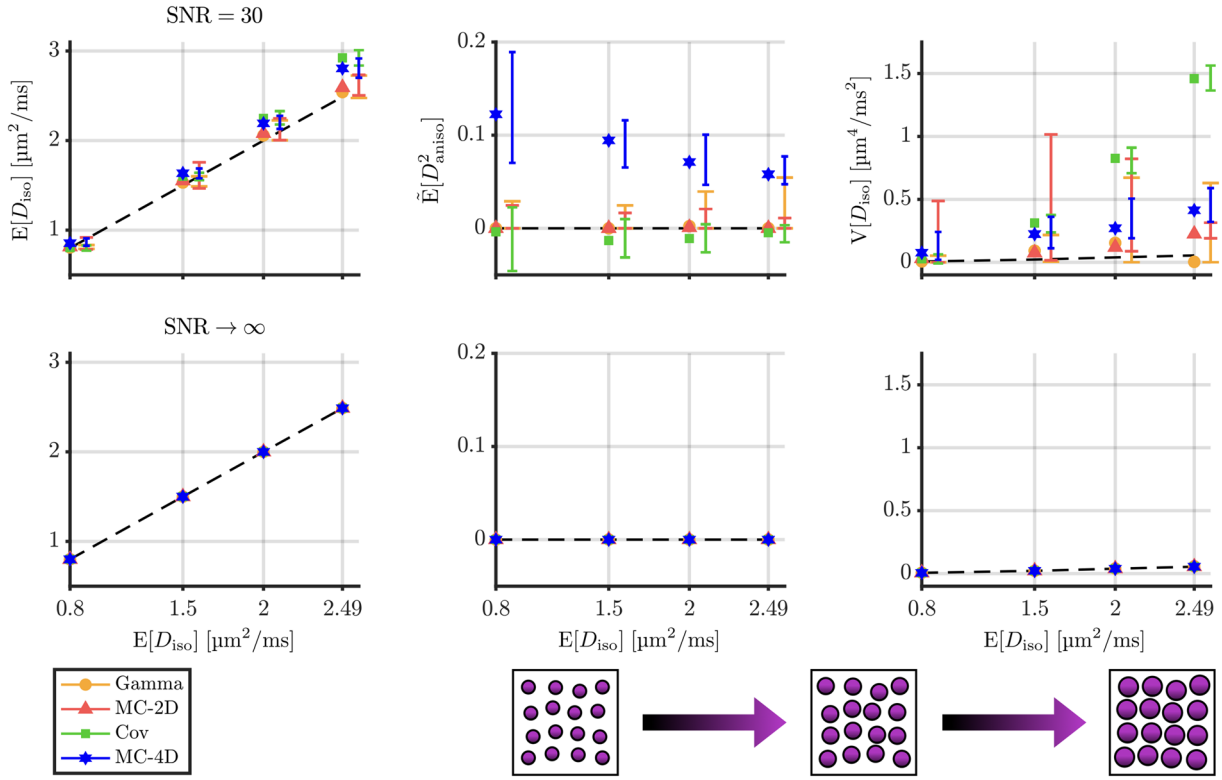

FIGURE 5 Performance of different inversion techniques in the characterization of an isotropic toy system consisting of a Gaussian distribution of diffusivities with varying mean but a constant standard-deviation-to-the-mean ratio of 0.1 µm²/ms. The properties of the simulated system—mean diffusivity E[D_{iso}], normalized mean squared anisotropy Ẽ[D^2_{aniso}], and variance of isotropic diffusivities V[D_{iso}]—were estimated by fitting the Gamma (orange circles), Cov (green squares), MC-2D (red triangles), and MC-4D (blue stars) algorithms to 100 different signal realizations simulated with either finite (top) or infinite (bottom) SNR. The various descriptors are plotted as a function of E[D_{iso}], with symbols indicating the medians of the descriptors across 100 inversions, shifted error bars representing the interquartile ranges (IQRs) that separate the first quartile from the third quartile across 100 inversions, and black dashed lines denoting the ground-truth descriptors. The bottom right panels illustrate the diffusion tensor distributions of the voxel contents investigated

not detected at finite SNR, and are instead replaced by the high-E[D_{iso}] and low-V[D_{iso}] biases that were already observed in Figure 5. Despite their limitations, both Gamma and Cov estimate Ẽ[D^2_{aniso}] accurately at high or low E[D_{iso}] (with Cov allowing negative anisotropy parameters, as in Figure 5). The Monte Carlo inversions do not show any infinite-SNR bias, but do exhibit finite-SNR biases at low E[D_{iso}] that increase with increasing V[D_{iso}]. This can be understood by the fact that generating isotropic variance implies giving more weight to intravoxel diffusional components with isotropic diffusivities both lower and higher than E[D_{iso}]. Hence, at low E[D_{iso}] and high V[D_{iso}], the *in silico* dataset comprises slow-diffusing components that present little signal contrast with the moderate b-values used in this study. This means that, at low SNR, the MC-4D method cannot tease apart the slow-diffusing components and overestimates E[D_{iso}], which in turn leads to an overestimation of both Ẽ[D^2_{aniso}] and V[D_{iso}]. These inaccuracies are reduced significantly at high E[D_{iso}], where the MC-4D method captures V[D_{iso}]accurately and presents a much reduced bias in Ẽ[D^2_{aniso}]. The bias reduction in Ẽ[D^2_{aniso}] originates from the upper physical bound that is imposed on the random axial and radial diffusivities generated by the Monte Carlo algorithms; this upper bound limits the maximal anisotropy of the high-E[D_{iso}] sampled configurations. Shifting our focus to the model-free inversion of powder-average signals, we observe that MC-2D tends to have a significantly lower precision than other methods when estimating E[D_{iso}] and V[D_{iso}], but captures Ẽ[D^2_{aniso}] accurately.

4.3 | Varying anisotropy with and without orientational order

Figure 7 shows the accuracy and precision of the signal inversion algorithms investigated for anisotropic unimodal systems with varying normalized mean anisotropy Ẽ[D^2_{aniso}]; while panel A focuses on orientationally ordered systems, panel B presents orientationally dispersed systems. Notice that, unlike other measures of anisotropy such as fractional anisotropy (FA),[5] Ẽ[D^2_{aniso}] is not affected by the degree of orientational order and is directly proportional to the underlying subvoxel anisotropy.[69] All diffusional components in Figure 7 share the same value of D_{iso}, which, according to Equation (5), implies Ẽ[D^2_{aniso}] = E[D^2_{Δ}]. For the most anisotropic system, the first-order signal deviation from monoexponentiality is quantified as (4/5) Ẽ[D^2_{aniso}] E[D_{iso}]² = 0.29 µm⁴/ms² (see Equation (11)).

Gamma exhibits similar results for both oriented and orientationally dispersed systems: it can quantify anisotropy accurately, except for extremely high values of Ẽ[D^2_{aniso}], where infinite-SNR biases are observed. Similar infinite-SNR biases were also observed for isotropic systems

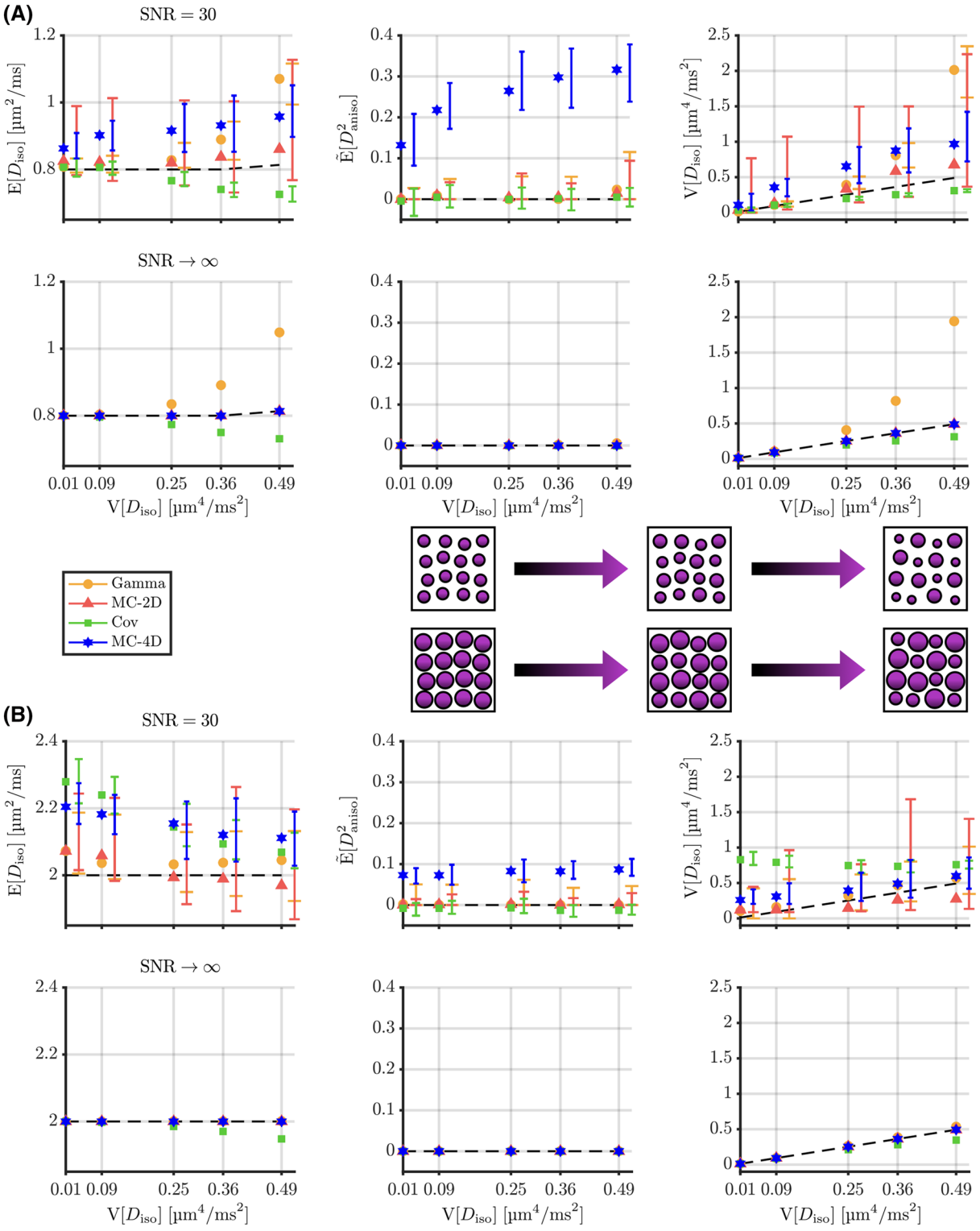

FIGURE 6 Performance of different inversion techniques in the characterization of two isotropic toy systems consisting of bimodal distributions of D_{iso} with a constant mean isotropic diffusivity E[D_{iso}] of (A) 0.8 µm^2/ms and (B) 2 µm^2/ms. Each toy system was devised as a sum of two Gaussian distributions with identical standard deviations (σ = 0.05 µm^2/ms). Symbol/color conventions are identical to those of Figure 5

with low E[D_{iso}] and high V[D_{iso}] (see Figure 6A), which indicates that the Gamma model cannot capture large deviations from monoexponentiality accurately. Gamma is not affected by orientational dispersion, because the powder-averaged signal associated with the acquisition scheme described in section 3.1 yields sufficient rotational invariance. Cov shows the same trends observed in the Gamma analysis, except for its infinite-SNR biases in orientationally dispersed systems containing microscopic domains of sufficiently high anisotropy. This can be understood by the fact that such systems are characterized by a "ski-slope" distribution (see the bottom panel of Figure 1A), wherein higher-than-second-order moments, not captured accurately by a cumulant expansion, are nonnegligible. Regarding MC-2D, it shows satisfying accuracy for all descriptors

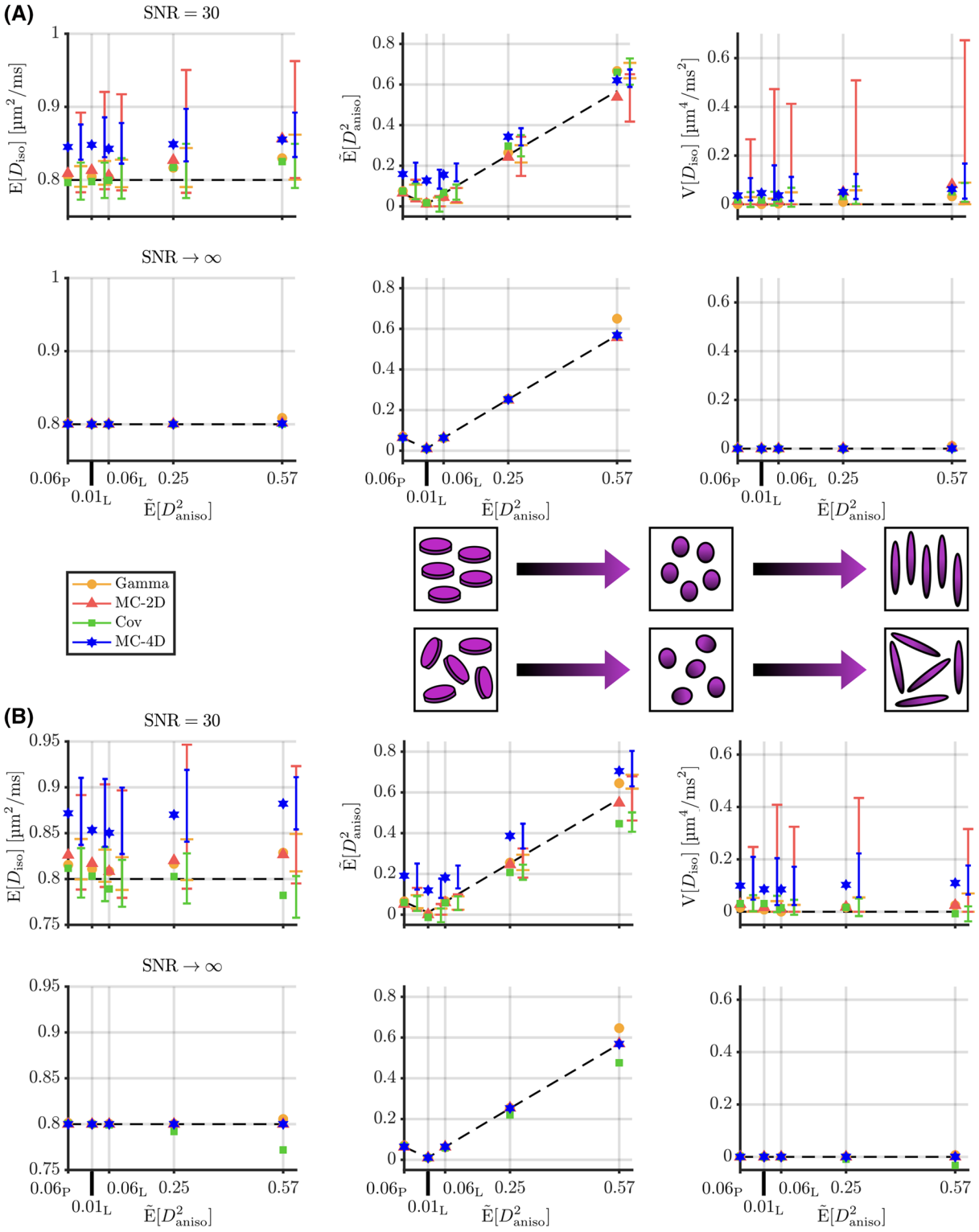

FIGURE 7 Descriptors of interest estimated by the inversion algorithms investigated as a function of the normalized mean anisotropy $\tilde{E}[D^2_{aniso}]$ for anisotropic toy systems consisting of (A) aligned and (B) orientationally dispersed anisotropic components, each of which is described by a unimodal distribution of D_Δ (Gaussian distribution) with constant $D_{iso} = 0.8$ μm²/ms and constant standard-deviation-to-the-mean ratio of 0.1. Orientationally dispersed systems are characterized by the order parameter $OP = E[P_2(\cos\beta)] = E[(3\cos^2\beta - 1)/2] = 0.01$. Notice that even though the first and third simulated systems exhibit the same normalized mean anisotropy, the former contains planar anisotropic components (subscript P) and the latter contains linear anisotropic components (subscript L). Symbol/color conventions are identical to those of Figure 5

but has low precision when estimating $E[D_{iso}]$ and $V[D_{iso}]$. Besides this, it is worth mentioning that MC-2D is very sensitive to the rotational invariance of the powder-averaged signal, as severe infinite-SNR biases appear when the powder-averaged signal is not truly rotationally invariant. A slight infinite-SNR bias is found in Figure 7A, because the acquisition scheme described in section 3.1 does not possess a perfectly

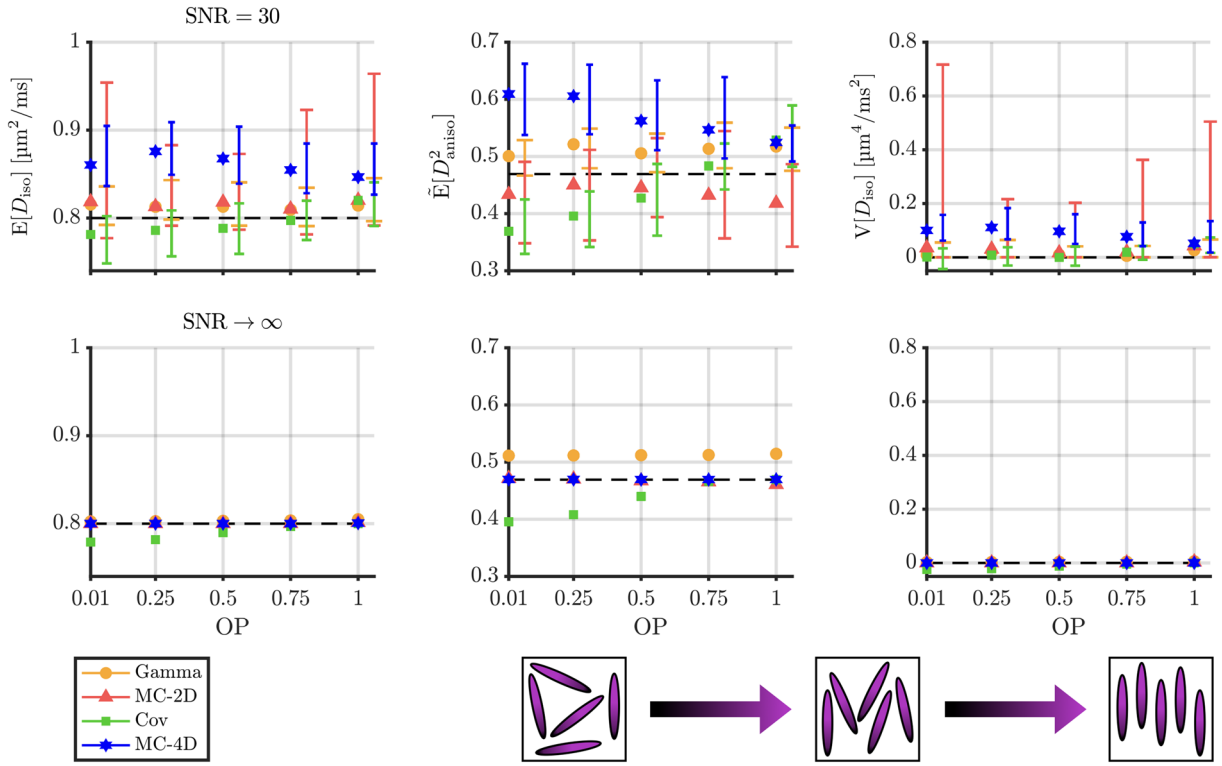

FIGURE 8 Descriptors of interest estimated by the investigated inversion algorithms as a function of the order parameter OP = E[$P_2(\cos\beta)$] for systems consisting of anisotropic components, each described by a unimodal distribution of D_Δ (Gaussian distribution) with constant D_{iso} = 0.8 μm²/ms and constant standard-deviation-to-the-mean ratio of 0.1. Each order parameter is fixed by orientating the anisotropic components following a given Watson distribution. These systems share common E[D_{iso}] = 0.8 μm²/ms, $\tilde{E}[D^2_{aniso}]$ = 0.47, and V[D_{iso}] = 0. Symbol/color conventions are identical to those of Figure 5

rotationally invariant powder average. Finally, MC-4D overestimates descriptors in both cases, but still preserves contrast and does not exhibit any infinite-SNR bias. The effects of intravoxel orientation dispersion alone are discussed in the next section.

4.4 | Orientational order and crossings

Figure 8 probes another degree of freedom of the diffusional size/shape/orientation 4D space, namely orientational order, with constant E[D_{iso}], $\tilde{E}[D^2_{aniso}]$, and V[D_{iso}]. Orientational order is quantified using the order parameter OP = E[$P_2(\cos\beta)$] = E[$(3\cos^2\beta - 1)/2$], where β is the angle between a component and the main eigenvector of the Saupe order tensor.[69,100] In particular, powder-like systems (OP → 0 and sufficiently high $\tilde{E}[D^2_{aniso}]$) can naturally arise in foodstuff,[81] colloidal systems,[100] and meningiomas.[74] Given the fact that the different systems studied share common E[D_{iso}] = 0.8 μm²/ms, $\tilde{E}[D^2_{aniso}]$ = 0.46, and V[D_{iso}] = 0, the system at OP = 1 matches a combination of the two last systems of Figure 7. Consequently, only changes occurring with decreasing orientational order remain to be discussed, as other trends were already discussed in section 4.3. Moreover, the effects of decreasing orientational order were observed to be analogous to those of increasing crossing angles between bundles of anisotropic components, meaning that the observations made in this section can also be used to understand the performance of the various analysis methods for systems consisting of crossing fibers.

The accuracy and precision of Gamma are unaffected by orientational order, as the powder average of signals associated with the acquisition scheme described in section 3.1 yields sufficient rotational invariance. Any bias of Gamma is here inherited from the high subvoxel anisotropy of the different systems, as shown in Figure 7. As for Cov, its infinite-SNR biases identified at low OP and high $\tilde{E}[D^2_{aniso}]$ in Figure 7B are now observed to develop progressively with decreasing OP, as the higher-than-second-order moments of the underlying DTD gain more relevance. MC-2D still presents the lowest precision, but exhibits an increased accuracy with decreasing orientational order that correlates with its infinite-SNR biases. This can be explained by the fact that the acquisition scheme described in section 3.1 does not possess a perfectly rotationally invariant powder average. This limitation becomes less and less relevant as the system itself becomes powder-like. Because the Gamma and MC-2D methods are both based on powder-averaged signals, one would expect the performance of both methods to be independent of OP. The fact that MC-2D shows a decreased accuracy at high OP, while Gamma does not, shows that the former method is more sensitive to errors in the powder-averaging procedure than the latter. Finally, MC-4D does not possess any infinite-SNR bias, but sees its finite-SNR accuracy decrease with decreasing orientational order. This is due to the fact that fitting becomes more challenging when the subvoxel microstructure comprises multiple relevant orientations.

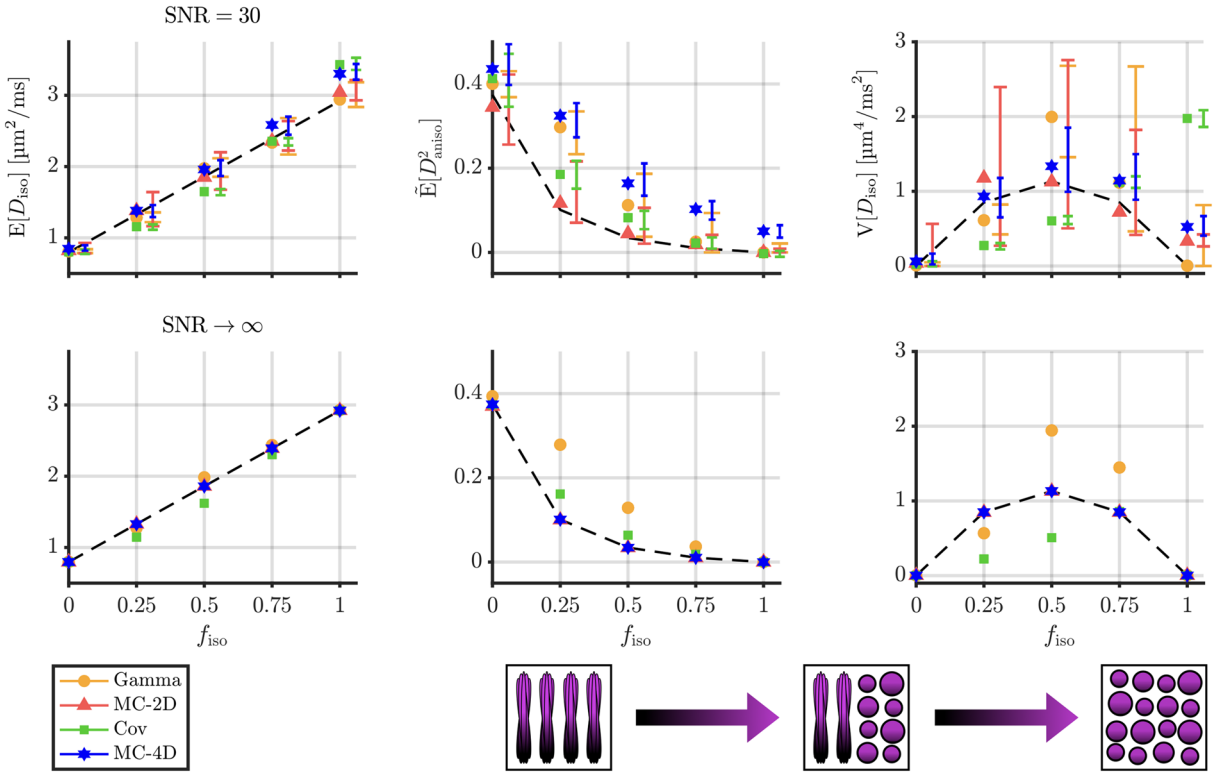

FIGURE 9 Descriptors of interest estimated by the inversion algorithms investigated as a function of the signal fraction $f_{iso} \in [0, 1]$ of an isotropic cerebrospinal-fluid-like structure (Gaussian distribution of D_{iso} with mean 3 μm²/ms and standard deviation 0.1 μm²/ms), starting from a voxel containing a fiber-like structure. This anisotropic structure is made of a Watson distribution of anisotropic components with an internal distribution of $D_{\parallel}$ (Gaussian distribution centered at 1.77 μm²/ms) and $D_{\perp}$ (Gaussian distribution centered at 0.31 μm²/ms). The diffusivities used come from multiple white-matter fiber estimations of the Magic DIAMOND model.[23,24,104] The Watson distribution is set to an intermediate order parameter OP = 0.4 to mimic some fiber dispersion. Symbol/color conventions are identical to those of Figure 5

4.5 | Varying fractions of isotropic and anisotropic components

Figure 9 presents the accuracy and precision of the signal inversion techniques investigated for systems shifting progressively from a single fiber-like voxel content to a cerebrospinal-fluid-like voxel content; these systems mimic the progression of damage in a single white matter system with intermediate orientational order. This shift is quantified by the signal fraction f_{iso} of the isotropic environment. The changes occurring between these composite systems are summed up here:

$$\begin{cases} \text{System 1} \\ f_{fiber} = 1 \\ f_{iso} = 0 \\ \mathrm{E}[D_{iso}] = 0.8 \\ \tilde{\mathrm{E}}[D^2_{aniso}] = 0.37 \\ \mathrm{V}[D_{iso}] = 1.84 \times 10^{-3} \end{cases} \quad \begin{cases} \text{System 2} \\ f_{fiber} = 0.75 \\ f_{iso} = 0.25 \\ \mathrm{E}[D_{iso}] = 1.32 \\ \tilde{\mathrm{E}}[D^2_{aniso}] = 0.1 \\ \mathrm{V}[D_{iso}] = 0.85 \end{cases} \quad \begin{cases} \text{System 3} \\ f_{fiber} = 0.5 \\ f_{iso} = 0.5 \\ \mathrm{E}[D_{iso}] = 1.86 \\ \tilde{\mathrm{E}}[D^2_{aniso}] = 0.03 \\ \mathrm{V}[D_{iso}] = 1.13 \end{cases} \quad \begin{cases} \text{System 4} \\ f_{fiber} = 0.25 \\ f_{iso} = 0.75 \\ \mathrm{E}[D_{iso}] = 2.39 \\ \tilde{\mathrm{E}}[D^2_{aniso}] = 0.01 \\ \mathrm{V}[D_{iso}] = 0.85 \end{cases} \quad \begin{cases} \text{System 5} \\ f_{fiber} = 0 \\ f_{iso} = 1 \\ \mathrm{E}[D_{iso}] = 3 \\ \tilde{\mathrm{E}}[D^2_{aniso}] = 0 \\ \mathrm{V}[D_{iso}] = 3.7 \times 10^{-3} \end{cases} \tag{27}$$

where $\mathrm{E}[D_{iso}]$ is expressed in μm²/ms and $\mathrm{V}[D_{iso}]$ is expressed in μm⁴/ms². Going from system 1 to system 5, $\mathrm{E}[D_{iso}]$ increases and the mean anisotropy decreases. As for isotropic variance, it increases between systems 1 and 3 and decreases between systems 3 and 5. Here, all results related to accuracy and precision can be understood from previous sections, so that only the contrasts captured by the inversion techniques remain to be discussed.

All investigated methods capture changes in $\mathrm{E}[D_{iso}]$ as a function of f_{iso} accurately, with comparable levels of accuracy and precision. Similarly, all methods capture the monotonic decrease of $\tilde{\mathrm{E}}[D^2_{aniso}]$ with increasing f_{iso}. While they share comparable precisions, the highest finite-SNR accuracy is obtained by MC-2D and the lowest finite-SNR accuracy is yielded by MC-4D. Finally, only MC-2D and MC-4D capture the changes in $\mathrm{V}[D_{iso}]$ as a function of f_{iso}. They present, respectively, low and intermediate precision.

5 | CONCLUSION AND OUTLOOK

We investigated how the accuracy and precision of multidimensional signal inversion algorithms behave in multiple systems varying in terms of mean diffusivity, variance of isotropic diffusivities, mean squared diffusion anisotropy, orientational order, and fractions of isotropic and

anisotropic components. The Gamma distribution fitting (Gamma) quantifies changes induced by $E[D_{iso}]$ and is robust to orientational dispersion, but does not capture large signal deviations from monoexponentiality, originating from either isotropic variance or anisotropy, accurately. The validity of the two-term covariance tensor approximation (Cov) is inherently limited by the $\mathbf{b} : \langle \mathbf{D} \rangle \to 0$ condition, which breaks down at high $E[D_{iso}]$ or b-values. For those values, Cov becomes very noise-sensitive and its accuracy decreases significantly. At low $E[D_{iso}]$, it quantifies changes due to anisotropy in systems with high orientational order but describes systems with intermediate to large isotropic variance inaccurately. Furthermore, Cov is not robust to orientational dispersion, because the underlying DTD of orientationally dispersed anisotropic components features nonnegligible higher-than-second-order moments that cannot be captured by a cumulant expansion. Nonetheless, Cov yields very fast inversions, as it can be recast into a linear problem tractable via mere matrix pseudoinversion. As for the 2D Monte Carlo inversion (MC-2D), it possesses a lower precision than other techniques, but nonetheless exhibits high accuracy for all the cases studied in this work. The major limitation in terms of accuracy is that this technique requires a rotationally invariant powder-averaged signal. Otherwise, biases appear even at infinite SNR for orientationally ordered voxel contents. Regarding the 4D Monte Carlo inversion (MC-4D), it overestimates all descriptors of interest in isotropic systems, because its sensitivity to noise translates as an additional anisotropy. This overestimation was observed to worsen in orientationally dispersed anisotropic systems, because it becomes difficult to tease apart the multiple relevant orientations of the subvoxel microstructure within the acquisition noise. Despite these limitations, MC-4D captures good contrast for all descriptors in the systems investigated and is the only technique that does not exhibit any infinite-SNR bias.

It is important to mention that all observations made in this article depend critically on the design of the acquisition scheme. Indeed, besides the aforementioned effect of rotational invariance of the powder-averaged signal, preliminary work by the present authors indicates that the performance of the various methods is affected by the choice of acquired coordinates $(b, b_\Delta, \Theta, \Phi)$, especially for Monte Carlo inversion techniques. For instance, removing the $b = 0$ signal from the acquisition scheme chosen in the present study, which is not conventional in the clinical setting, causes MC-4D to exhibit infinite-SNR biases at high $V[D_{iso}]$ in the systems shown in Figure 6. This is due to the fact that our two lowest non-zero b-values, 100 and 700 s/mm^2, cannot capture alone the initial signal decay at low b-value. Interestingly, acquisition schemes containing planar b tensors ($b_\Delta = -0.5$) have been shown to increase precision in parameter estimation in both biophysical models and signal representations of white-matter tissues.[101,102] Although outside the scope of this present work, a comprehensive study of the link between experimental design and inversion performance should be pursued nonetheless. Alternative analysis procedures and improvements to the methods studied should also be investigated.

First, developing a Gamma equivalent of the covariance tensor approximation, that is, considering a matrix-variate Gamma distribution[23,24,103,104] in order to constrain the solution space to physical solutions, could prove useful. Second, previous studies have shown that denoising techniques[105] can improve the precision of parameters estimated from the Laplace inversion of MRI relaxometry data.[106] Assuming that similar denoising algorithms can be translated directly to tensor-valued diffusion data, they may improve the performance of the algorithms studied in this article. The MC-4D method in particular could gain a huge boost in accuracy, as it does not possess any infinite-SNR bias and most of its limitations stem from its sensitivity to noise in the data. Finally, regularization techniques have traditionally been used to constrain the solution space of various diffusion and relaxation signal inversion techniques.[88,90,107,108] Whether or not such regularization constraints improve the inversion of tensor-valued data is a question that remains to be addressed.

Despite the protocol dependence of our present study, let us propose the following take-home message. The Gamma distribution fitting grants a versatile inversion that retrieves accurate statistical descriptors of the intravoxel diffusion tensor distribution as long as the powder-averaged signal does not deviate severely from monoexponentiality. The covariance tensor approximation shares many limitations of the Gamma distribution fitting, but offers fast inversions that render it practical for immediate, yet preliminary, clinical assessment of tissue microstructure. Nevertheless, one should avoid studying anisotropic tissues with low orientational order, such as edematous white-matter tissues and certain meningiomas. Regarding these two inversion methods, preliminary work suggests that their infinite-SNR biases are intrinsic, which indicates that only limited improvement will be achieved by optimizing the acquisition scheme. In contrast, Monte Carlo inversion techniques are slow, but do not present infinite-SNR biases when applied to reasonable clinical protocols, which suggests that their true potential is yet to be reached, upon reduction of the effect of noise. Nonetheless, the 2D Monte Carlo inversion, the accuracy of which depends strongly on the rotational invariance of the powder-averaged signal and the precision of which is remarkably lower than that of other inversion techniques, should be avoided. As for the 4D Monte Carlo inversion, it may still preserve contrast despite its finite-SNR biases and is the only one that can access fiber-specific information,[92] making it promising on the one hand for clinical assessment of tissue microstructure and on the other hand for future studies of both neurodevelopment and neurodegeneration.

ACKNOWLEDGMENTS

This work was financially supported by the Swedish Foundation for Strategic Research (ITM17-0267) and the Swedish Research Council (2018-03697). Daniel Topgaard owns shares in Random Walk Imaging AB (Lund, Sweden, http://www.rwi.se/), holding patents related to the methods described. We warmly thank Filip Szczepankiewicz and Markus Nilsson for fruitful discussions.

ORCID

Alexis Reymbaut https://orcid.org/0000-0002-2167-5483
Daniel Topgaard https://orcid.org/0000-0001-9373-6348

REFERENCES

1. Norris DG. The effects of microscopic tissue parameters on the diffusion weighted magnetic resonance imaging experiment. *NMR Biomed*. 2001;14(2):77-93. http://doi.org/10.1002/nbm.682
2. Sehy JV, Ackerman JJ, Neil JJ. Evidence that both fast and slow water ADC components arise from intracellular space. *Magn Reson Med*. 2002;48(5):765-770. http://doi.org/10.1002/mrm.10301
3. Minati L, foundations WWP. Physical models, and methods of diffusion magnetic resonance imaging of the brain. *Rev Concepts Magn Reson A*. 2007;30A(5):278-307. http://doi.org/10.1002/cmr.a.20094
4. Mulkern RV, Haker SJ, Maier SE. On high b diffusion imaging in the human brain: ruminations and experimental insights. *Magn Reson Imaging*. 2009;27(8):1151-1162. http://doi.org/10.1016/j.mri.2009.05.003
5. Basser PJ, Microstructural PC. physiological features of tissues elucidated by quantitative-diffusion-tensor. *MRI J Magn Reson, Ser B*. 1996;111(3):209-219. http://doi.org/10.1006/jmrb.1996.0086
6. Alexander AL, Hasan KM, Lazar M, Tsuruda JS, Parker DL. Analysis of partial volume effects in diffusion-tensor MRI. *Magn Reson Med*. 2001;45(5):770-780. http://doi.org/10.1002/mrm.1105
7. Alexander AL, Lee JE, Lazar M, Field AS. Diffusion tensor imaging of the brain. *Neurother*. 2007;4(3):316-329. http://doi.org/10.1016/j.nurt.2007.05.011
8. Jones DK, Cercignani M. Twenty-five pitfalls in the analysis of diffusion MRI data. *NMR Biomed*. 2010;23(7):803-820. http://doi.org/10.1002/nbm.1543
9. Jones DK, Knösche TR, integrity TR, count fiber, fallacies other. White matter The do's and don'ts of diffusion MRI. *NeuroImage*. 2013;73:239-254. https://doi.org/10.1016/j.neuroimage.2012.06.081
10. Tuch DS, Reese TG, Wiegell MR, Makris N, Belliveau JW, Wedeen VJ. High angular resolution diffusion imaging reveals intravoxel white matter fiber heterogeneity. *Magn Reson Med*. 2002;48(4):577-582. http://doi.org/10.1002/mrm.10268
11. Yablonskiy DA, Bretthorst GL, Ackerman JJ. Statistical model for diffusion attenuated MR signal. *Magn Reson Med*. 2003;50(4):664-669. http://doi.org/10.1002/mrm.10578
12. Kroenke CD, Ackerman JJ, Yablonskiy DA. On the nature of the NAA diffusion attenuated MR signal in the central nervous system. *Magn Reson Med*. 2004;52(5):1052-1059. http://doi.org/10.1002/mrm.20260
13. Jian B, Vemuri BC, Özarslan E, Carney PR, Mareci TH. A novel tensor distribution model for the diffusion-weighted MR signal. *NeuroImage*. 2007;37(1):164-176. http://doi.org/10.1016/j.neuroimage.2007.03.074
14. Jespersen SN, Kroenke CD, Østergaard L, Ackerman JJ, Yablonskiy DA. Modeling dendrite density from magnetic resonance diffusion measurements. *NeuroImage*. 2007;34(4):1473-1486. http://doi.org/10.1016/j.neuroimage.2006.10.037
15. Leow AD, Zhu S, Zhan L, et al. The tensor distribution function. *Magn Reson Med*. 2009;61(1):205-214. http://doi.org/10.1002/mrm.21852
16. Pasternak O, Sochen N, Gur Y, Intrator N, Assaf Y. Free water elimination and mapping from diffusion MRI. *Magn Reson Med*. 2009;62(3):717-730. http://doi.org/10.1002/mrm.22055
17. Wang Y, Wang Q, Haldar JP, et al. Quantification of increased cellularity during inflammatory demyelination. *Brain*. 2011;134(12):3590-3601. http://doi.org/10.1093/brain/awr307
18. Fieremans E, Jensen JH, Helpern JA. White matter characterization with diffusional kurtosis imaging. *NeuroImage*. 2011;58(1):177-188. http://doi.org/10.1016/j.neuroimage.2011.06.006
19. Zhang H, Schneider T, Wheeler-Kingshott CA, Alexander DC. NODDI Practical in vivo neurite orientation dispersion and density imaging of the human brain. *NeuroImage*. 2012;61(4):1000-1016. http://doi.org/10.1016/j.neuroimage.2012.03.072
20. Jelescu IO, Veraart J, Fieremans E, Novikov DS. Degeneracy in model parameter estimation for multi-compartmental diffusion in neuronal tissue. *NMR Biomed*. 2016;29(1):33-47. NBM-15-0204.R2 http://doi.org/10.1002/nbm.3450
21. Kaden E, Kelm ND, Carson RP, Does MD, Alexander DC. Multi-compartment microscopic diffusion imaging. *NeuroImage*. 2016;139:346-359. http://doi.org/10.1016/j.neuroimage.2016.06.002
22. Westin CF, Knutsson H, Pasternak O, et al. Q-space trajectory imaging for multidimensional diffusion MRI of the human brain. *NeuroImage*. 2016;135:345-362. http://doi.org/10.1016/j.neuroimage.2016.02.039
23. Scherrer B, Schwartzman A, Taquet M, Sahin M, Prabhu SP, Warfield SK. Characterizing brain tissue by assessment of the distribution of anisotropic microstructural environments in diffusion-compartment imaging (DIAMOND). *Magn Reson Med*. 2016;76(3):963-977. http://doi.org/10.1002/mrm.25912
24. Scherrer B, Taquet M, Schwartzman A, St-Onge E, Rensonnet G, Prabhu SP, Warfield SK. Decoupling axial and radial tissue heterogeneity in diffusion compartment imaging. In: Information Processing in Medical Imaging (IPMI) Springer, Cham; 2017:440-452.
25. Lampinen B, Szczepankiewicz F, Mårtensson J, Westen vD, Sundgren PC. Neurite density imaging versus imaging of microscopic anisotropy in diffusion MRI: A model comparison using spherical tensor encoding. *NeuroImage*. 2017;147:517-531. http://doi.org/10.1016/j.neuroimage.2016.11.053
26. Reisert M, Kellner E, Dhital B, Hennig J, Kiselev VG. Disentangling micro from mesostructure by diffusion MRI: A Bayesian approach. *NeuroImage*. 2017;147:964-975. http://doi.org/10.1016/j.neuroimage.2016.09.058
27. Novikov DS, Kiselev VG, Jespersen SN. *On modeling Magn Reson Med*. 2018;79(6):3172-3193. http://doi.org/10.1002/mrm.27101
28. Novikov DS, Fieremans E, Jespersen SN, Kiselev VG. Quantifying brain microstructure with diffusion MRI: Theory and parameter estimation. *NMR Biomed*. 2018;0(0):e3998. http://doi.org/10.1002/nbm.3998
29. Rensonnet G, Scherrer B, Warfield SK, Macq B, Taquet M. Assessing the validity of the approximation of diffusion-weighted-MRI signals from crossing fascicles by sums of signals from single fascicles. *Magn Reson Med*. 2018;79(4):2332-2345. http://doi.org/10.1002/mrm.26832
30. Eriksson S, Lasic S, Nilsson M, Westin CF, Topgaard D. NMR diffusion-encoding with axial symmetry and variable anisotropy: Distinguishing between prolate and oblate microscopic diffusion tensors with unknown orientation distribution. *J Chem Phys*. 2015;142(10):104201. http://doi.org/10.1063/1.4913502

31. Topgaard D. Multidimensional diffusion MRI. *J Magn Reson*. 2017;275:98-113. http://doi.org/10.1016/j.jmr.2016.12.007
32. Basser P, Mattiello J, LeBihan D. MR diffusion tensor spectroscopy and imaging. *Biophys J*. 1994;66(1):259-267. http://doi.org/10.1016/S0006-3495(94)80775-1
33. Mattiello J, Basser P, Lebihan D. Analytical expressions for the b matrix in NMR diffusion imaging and spectroscopy. *J Magn Reson Ser A*. 1994;108(2):131-141. http://doi.org/10.1006/jmra.1994.1103
34. Mattiello J, Basser PJ, Le Bihan D. The b matrix in diffusion tensor echo-planar imaging. *Magn Reson Med*. 1997;37(2):292-300. http://doi.org/10.1002/mrm.1910370226
35. Woessner DE. NMR spin-echo self-diffusion measurements on fluids undergoing restricted diffusion. *J Phys Chem*. 1963;67(6):1365-1367. http://doi.org/10.1021/j100800a509
36. Johnson CS. Effects of chemical exchange in diffusion-ordered 2D NMR spectra. *J Magn Reson Ser A*. 1993;102(2):214-218. http://doi.org/10.1006/jmra.1993.1093
37. Van AT, Holdsworth SJ, Bammer R. In vivo investigation of restricted diffusion in the human brain with optimized oscillating diffusion gradient encoding. *Magn Reson Med*. 2014;71(1):83-94. http://doi.org/10.1002/mrm.24632
38. Baron CA, Beaulieu C. Oscillating gradient spin-echo (OGSE) diffusion tensor imaging of the human brain. *Magn Reson Med*. 2014;72(3):726-736. http://doi.org/10.1002/mrm.24987
39. Baron CA, Kate M, Gioia L, et al. Reduction of diffusion-weighted imaging contrast of acute ischemic stroke at short diffusion times. *Stroke*. 2015;46(8):2136-2141. http://doi.org/10.1161/STROKEAHA.115.008815
40. Fieremans E, Burcaw LM, Lee HH, Lemberskiy G, Veraart J, Novikov DS. In vivo observation and biophysical interpretation of time-dependent diffusion in human white matter. *NeuroImage*. 2016;129:414-427. http://doi.org/10.1016/j.neuroimage.2016.01.018
41. Veraart J, Fieremans E, Novikov DS. On the scaling behavior of water diffusion in human brain white matter. *NeuroImage*. 2019;185:379-387. http://doi.org/10.1016/j.neuroimage.2018.09.075
42. Lundell H, Nilsson M, Dyrby TB, et al. Multidimensional diffusion MRI with spectrally modulated gradients reveals unprecedented microstructural detail. *Sci Rep*. 2019;9(1):9026. http://doi.org/10.1038/s41598-019-45235-7
43. Jespersen SN, Olesen JL, Hansen B, Shemesh N. Diffusion time dependence of microstructural parameters in fixed spinal cord. *NeuroImage*. 2018;182:329-342. Microstructural Imaging http://doi.org/10.1016/j.neuroimage.2017.08.039
44. Grussu F, Ianuş A, Tur C, et al. Relevance of time-dependence for clinically viable diffusion imaging of the spinal cord. *Magn Reson Med*. 2019;81(2):1247-1264. http://doi.org/10.1002/mrm.27463
45. Lemberskiy G, Rosenkrantz AB, Veraart J, Taneja SS, Novikov DS, Fieremans E. Time-dependent diffusion in prostate cancer. *Investig Radiol*. 2017;52(7):405-411. http://doi.org/10.1097/RLI.0000000000000356
46. Lemberskiy G, Fieremans E, Veraart J, Deng FM, Rosenkrantz AB, Novikov DS. Characterization of prostate microstructure using water diffusion and NMR relaxation. *Front Phys*. 2018;6:91. http://doi.org/10.3389/fphy.2018.00091
47. Clark CA, Hedehus M, Moseley ME. Diffusion time dependence of the apparent diffusion tensor in healthy human brain and white matter disease. *Magn Reson Med*. 2001;45(6):1126-1129. http://doi.org/10.1002/mrm.1149
48. Ronen I, Moeller S, Ugurbil K, Kim DS. Analysis of the distribution of diffusion coefficients in cat brain at 9.4 T using the inverse Laplace transformation. *Magn Reson Imaging*. 2006;24(1):61-68. http://doi.org/10.1016/j.mri.2005.10.023
49. Nilsson M, Lätt J, Nordh E, Wirestam R, Ståhlberg F, Brockstedt S. On the effects of a varied diffusion time in vivo: is the diffusion in white matter restricted? *Magn Reson Imaging*. 2009;27(2):176-187. http://doi.org/10.1016/j.mri.2008.06.003
50. Nilsson M, Lätt J, Westen vD. Noninvasive mapping of water diffusional exchange in the human brain using filter-exchange imaging. *Magn Reson Med*. 2013;69(6):1572-1580. http://doi.org/10.1002/mrm.24395
51. Nilsson M, Westen vD, Ståhlberg F, Sundgren PC, Lätt J. The role of tissue microstructure and water exchange in biophysical modelling of diffusion in white matter. *Magn Reson Mater Phys Biol Med*. 2013;26(4):345-370. http://doi.org/10.1007/s10334-013-0371-x
52. Santis SD, Jones DK, Roebroeck A. Including diffusion time dependence in the extra-axonal space improves in vivo estimates of axonal diameter and density in human white matter. *NeuroImage*. 2016;130(Suppl C):91-103. http://doi.org/10.1016/j.neuroimage.2016.01.047
53. Lampinen B, Szczepankiewicz F, Westen vD, et al. Optimal experimental design for filter exchange imaging: Apparent exchange rate measurements in the healthy brain and in intracranial tumors. *Magn Reson Med*. 2017;77(3):1104-1114. http://doi.org/10.1002/mrm.26195
54. Veraart J, Novikov DS, Fieremans E. TE dependent Diffusion Imaging (TEdDI) distinguishes between compartmental T2 relaxation times. *Microstructural Imaging*. 2018;182:360-369. http://doi.org/10.1016/j.neuroimage.2017.09.030
55. Tournier JD, Calamante F, Gadian DG, Connelly A. Direct estimation of the fiber orientation density function from diffusion-weighted MRI data using spherical deconvolution. *NeuroImage*. 2004;23(3):1176-1185. http://doi.org/10.1016/j.neuroimage.2004.07.037
56. Tournier JD, Calamante F, Connelly A. Robust determination of the fibre orientation distribution in diffusion MRI. *Non-negativity constrained super-resolved spherical deconvolution NeuroImage*. 2007;35(4):1459-1472. http://doi.org/10.1016/j.neuroimage.2007.02.016
57. Topgaard D. Multiple dimensions for random walks. *J Magn Reson*. 2019;306:150-154. http://doi.org/10.1016/j.jmr.2019.07.024
58. Topgaard D. NMR methods for studying microscopic diffusion anisotropy. *Diffusion NMR of confined systems: Fluid transport in porous solids and heterogeneous naterials, new developments in NMR*; 2016:226-259.
59. Provencher SW. A constrained regularization method for inverting data represented by linear algebraic or integral equations. *Comput Phys Commun*. 1982;27(3):213-227. http://doi.org/10.1016/0010-4655(82)90173-4
60. Kroeker RM, Henkelman RM. Analysis of biological NMR relaxation data with continuous distributions of relaxation times. *J Magn Reson (1969)*. 1986;69(2):218-235. http://doi.org/10.1016/0022-2364(86)90074-0
61. Whittall KP, MacKay AL. Quantitative interpretation of NMR relaxation data. *J Magn Reson (1969)*. 1989;84(1):134-152. http://doi.org/10.1016/0022-2364(89)90011-5
62. Cory DG, Garroway AN, Miller JB. Applications of spin transport as a probe of local geometry. *Polymer Prepr*. 1990;31:149-150.

63. Mitra PP. Multiple wave-vector extensions of the NMR pulsed-field-gradient spin-echo diffusion measurement. *Phys Rev B*. 1995;51:15074-15078. http://doi.org/10.1103/PhysRevB.51.15074
64. Callaghan PT, Furó I.. Diffusion-diffusion correlation and exchange as a signature for local order and dynamics. *J Chem Phys*. 2004;120(8):4032-4038. http://doi.org/10.1063/1.1642604
65. Eriksson S, Lasic S, Topgaard D. Isotropic diffusion weighting in PGSE NMR by magic-angle spinning of the q-vector. *J Magn Reson*. 2013;226:13-18. http://doi.org/10.1016/j.jmr.2012.10.015
66. de Almeida Martins JP, Topgaard D. Two-dimensional correlation of isotropic and directional diffusion using NMR. *Phys Rev Lett*. 2016;116:087601. http://doi.org/10.1103/PhysRevLett.116.087601
67. de Almeida Martins JP, Topgaard D. Multidimensional correlation of nuclear relaxation rates and diffusion tensors for model-free investigations of heterogeneous anisotropic porous materials. *Sci Rep*. 2488;8(1):2018. http://doi.org/10.1038/s41598-018-19826-9
68. Topgaard D. Diffusion tensor distribution imaging. *NMR Biomed*. 2019;32(5):e4066. http://doi.org/10.1002/nbm.4066
69. Lasic S, Szczepankiewicz F, Eriksson S, Nilsson M, Topgaard D. Microanisotropy imaging: quantification of microscopic diffusion anisotropy and orientational order parameter by diffusion MRI with magic-angle spinning of the q-vector. *Front Phys*. 2014;2:11. http://doi.org/10.3389/fphy.2014.00011
70. Lawrenz M, Koch MA, Finsterbusch J. A tensor model and measures of microscopic anisotropy for double-wave-vector diffusion-weighting experiments with long mixing times. *J Magn Reson*. 2010;202(1):43-56. http://doi.org/10.1016/j.jmr.2009.09.015
71. Jespersen SN, Lundell H, Sønderby CK, Dyrby TB. Orientationally invariant metrics of apparent compartment eccentricity from double pulsed field gradient diffusion experiments. *NMR Biomed*. 2013;26(12):1647-1662. http://doi.org/10.1002/nbm.2999
72. Shemesh N, Jespersen SN, Alexander DC, et al. Conventions and nomenclature for double diffusion encoding NMR and MRI. *Magn Reson Med*. 2016;75(1):82-87. http://doi.org/10.1002/mrm.25901
73. Ianuş A, Jespersen SN, Duarte TS, Alexander DC, Drobnjak I, Shemesh N. Accurate estimation of microscopic diffusion anisotropy and its time dependence in the mouse brain. *NeuroImage*. 2018;183:934-949. http://doi.org/10.1016/j.neuroimage.2018.08.034
74. Szczepankiewicz F, Lasic S. Westen vD, others. Quantification of microscopic diffusion anisotropy disentangles effects of orientation dispersion from microstructure: Applications in healthy volunteers and in brain tumors. *NeuroImage*. 2015;104:241-252. http://doi.org/10.1016/j.neuroimage.2014.09.057
75. Szczepankiewicz F. Westen vD, Englund E, others. The link between diffusion MRI and tumor heterogeneity: Mapping cell eccentricity and density by diffusional variance decomposition (DIVIDE). *NeuroImage*. 2016;142:522-532. http://doi.org/10.1016/j.neuroimage.2016.07.038
76. Henriques RN, Jespersen SN, Shemesh N. Microscopic anisotropy misestimation in spherical-mean single diffusion encoding MRI. *Magn Reson Med*. 2019;81(5):3245-3261. http://doi.org/10.1002/mrm.27606
77. de Swiet TM, Mitra PP. Possible systematic errors in single-shot measurements of the trace of the diffusion tensor. *J Magn Reson Ser B*. 1996;111(1):15-22. http://doi.org/10.1006/jmrb.1996.0055
78. Jespersen SN, Olesen JL, Ianuş A, Shemesh N. Effects of nonGaussian diffusion on "isotropic diffusion" measurements: An ex-vivo microimaging and simulation study. *J Magn Reson*. 2019;300:84-94. http://doi.org/10.1016/j.jmr.2019.01.007
79. Szczepankiewicz F, Lasic S, Nilsson M, Lundell H, Westin CF, Topgaard D. Is spherical diffusion encoding rotation invariant?An investigation of diffusion time-dependence in the healthy brain. *Proc Intl Soc Mag Reson Med*. 2019;27:0223.
80. Lindblom G, Wennerström H, Arvidson G. Translational diffusion in model membranes studied by nuclear magnetic-resonance. *Int J Quant Chem*. 1977;12:153-158.
81. Callaghan P, Jolley K, Lelievre J. Diffusion of water in the endosperm tissue of wheat grains as studied by pulsed field gradient nuclear magnetic resonance. *Biophys J*. 1979;28(1):133-141. http://doi.org/10.1016/S0006-3495(79)85164-4
82. Edén M. Computer simulations in solid-state NMR. III. Powder averaging. *Concepts Magn Reson A*. 2003;18A(1):24-55. http://doi.org/10.1002/cmr.a.10065
83. Herberthson M, Yolcu C, Knutsson H, Westin CF, Özarslan E. Orientationally-averaged diffusion-attenuated magnetic resonance signal for locally-anisotropic diffusion. *Sci Rep*. 4899;9(1). http://doi.org/10.1038/s41598-019-41317-8
84. Koppel DE. Analysis of macromolecular polydispersity in intensity correlation spectroscopy: The method of cumulants. *J Chem Phys*. 1972;57(11):4814-4820. http://doi.org/10.1063/1.1678153
85. Röding M, Bernin D, Jonasson J, et al. The gamma distribution model for pulsed-field gradient NMR studies of molecular-weight distributions of polymers. *J Magn Reson*. 2012;222:105-111. http://doi.org/10.1016/j.jmr.2012.07.005
86. Nilsson M, Larsson J, Lundberg D, et al. Liquid crystal phantom for validation of microscopic diffusion anisotropy measurements on clinical MRI systems. *Magn Reson Med*. 2018;79(3):1817-1828. http://doi.org/10.1002/mrm.26814
87. Istratov AA, Vyvenko OF. Exponential analysis in physical phenomena. *Rev Sci Instrum*. 1999;70(2):1233-1257. http://doi.org/10.1063/1.1149581
88. Borgia G, Brown R, Fantazzini P. Uniform-penalty inversion of multiexponential decay data. *J Magn Reson*. 1998;132(1):65-77. http://doi.org/10.1006/jmre.1998.1387
89. Venkataramanan L, Song Y-Q, Hurlimann MD. Solving Fredholm integrals of the first kind with tensor product structure in 2 and 2.5 dimensions. *IEEE Trans Signal Proc*. 2002;50(5):1017-1026. http://doi.org/10.1109/78.995059
90. Chouzenoux É, Moussaoui S, Idier J, Mariette F. Efficient maximum entropy reconstruction of nuclear magnetic resonance T1–T2 spectra. *IEEE Trans Signal Proc*. 2010;58(12):6040-6051. http://doi.org/10.1109/TSP.2010.2071870
91. Mitchell J, Chandrasekera T, Gladden L. Numerical estimation of relaxation and diffusion distributions in two dimensions. *Progr Nucl Magn Reson Spectrosc*. 2012;62:34-50. http://doi.org/10.1016/j.pnmrs.2011.07.002
92. de Almeida Martins JP, Tax CMW, Mailhiot SE, et al. Mapping of fibre-specific relaxation and diffusivities in heterogeneous brain tissue. *Proc Intl Soc Mag Reson Med*. 2019;27:0162.
93. Nilsson M, Szczepankiewicz F, Lampinen B, et al. An open-source framework for analysis of multidimensional diffusion MRI data implemented in MATLAB. *Proc Intl Soc Mag Reson Med*. 2018;26:5355.

94. Nilsson M, Szczepankiewicz F, Topgaard D. MATLAB code for Multidimensional Diffusion MRI. *Accessed: July*. 2019:9. https://github.com/daniel-topgaard/md-dmri
95. Szczepankiewicz F, Sjölund J, Ståhlberg F, Lätt J, Nilsson M. Tensor-valued diffusion encoding for diffusional variance decomposition (DIVIDE): Technical feasibility in clinical MRI systems. *PLOS ONE*. 2019;14(3):1-20. http://doi.org/10.1371/journal.pone.0214238
96. Gudbjartsson H, Patz S. The Rician distribution of noisy MRI data. *Magn Reson Med*. 1995;34(6):910-914. http://doi.org/10.1002/mrm.1910340618
97. Jones DK. Basser PJ. "Squashing peanuts and smashing pumpkins": How noise distorts diffusion-weighted MR data. *Magn Reson Med*. 2004;52(5):979-993. http://doi.org/10.1002/mrm.20283
98. Gilbert G, Simard D, Beaudoin G. Impact of an improved combination of signals from array coils in diffusion tensor imaging. *IEEE Trans Med Imaging*. 2007;26(11):1428-1436. http://doi.org/10.1109/TMI.2007.907699
99. Sotiropoulos SN, Moeller S, Jbabdi S, et al. Effects of image reconstruction on fiber orientation mapping from multichannel diffusion MRI: Reducing the noise floor using SENSE. *Magn Reson Med*. 2013;70(6):1682-1689. http://doi.org/10.1002/mrm.24623
100. Topgaard D. Director orientations in lyotropic liquid crystals: diffusion MRI mapping of the Saupe order tensor. *Phys Chem Chem Phys*. 2016;18:8545-8553. http://doi.org/10.1039/C5CP07251D
101. Coelho S, Pozo JM, Jespersen SN, Jones DK, Frangi AF. Resolving degeneracy in diffusion MRI biophysical model parameter estimation using double diffusion encoding. *Magn Reson Med*. 2019;82(1):395-410. http://doi.org/10.1002/mrm.27714
102. Coelho S, Pozo JM, Jespersen SN, Frangi AF. Optimal experimental design for biophysical modelling in multidimensional diffusion MRI. In: International Conference on Medical Image Computing and Computer-Assisted Intervention Springer, Cham:617-625. arXiv e-prints 2019: arXiv:1907.06139.
103. Guptar AK, Nagar DK. *Matrix Variate Distributions*. Boca Raton: Florida: Chapman and Hall/CRC; 2000.
104. Reymbaut A, Gilbert G, Szczepankiewicz F, Nilsson M, Scherrer B, Descoteaux M. The "Magic DIAMOND" method: probing brain microstructure by combining b-tensor encoding and advanced diffusion compartment imaging. *Proc Intl Soc Mag Reson Med*. 2018;26:0257.
105. Veraart J, Novikov DS, Christiaens D, Ades-aron B, Sijbers J, Fieremans E. Denoising of diffusion MRI using random matrix theory. *NeuroImage*. 2016;142:394-406. http://doi.org/10.1016/j.neuroimage.2016.08.016
106. Does MD, Olesen JL, Harkins KD, et al. Evaluation of principal component analysis image denoising on multi-exponential MRI relaxometry. *Magn Reson Med*. 2019;81(6):3503-3514. http://doi.org/10.1002/mrm.27658
107. Benjamini D, Basser PJ. Use of marginal distributions constrained optimization (MADCO) for accelerated 2D MRI relaxometry and diffusometry. *J Magn Reson*. 2016;271:40-45. http://doi.org/10.1016/j.jmr.2016.08.004
108. Kim D, Doyle EK, Wisnowski JL, Kim JH, Haldar JP. Diffusion-relaxation correlation spectroscopic imaging: A multidimensional approach for probing microstructure. *Magn Reson Med*. 2017;78(6):2236-2249. http://doi.org/10.1002/mrm.26629

How to cite this article: Reymbaut A, Mezzani P, de Almeida Martins JP, Topgaard D. Accuracy and precision of statistical descriptors obtained from multidimensional diffusion signal inversion algorithms. *NMR in Biomedicine*. 2020;e4267. https://doi.org/10.1002/nbm.4267